# Mechanisms of Rainfall Biases in Two CORDEX-CORE Regional Climate Models at Rainfall Peaks over Central Equatorial Africa

ALAIN T. TAMOFFO,[a,b] LEONARD K. AMEKUDZI,[a] TORSTEN WEBER,[c] DERBETINI A. VONDOU,[b] EDMUND I. YAMBA,[a] AND DANIELA JACOB[c]

[a] *Physics Department, Kwame Nkrumah University of Science and Technology, Kumasi, Ghana*
[b] *Laboratory for Environmental Modelling and Atmospheric Physics (LEMAP), Physics Department, University of Yaoundé I, Yaoundé, Cameroon*
[c] *Climate Service Center Germany (GERICS), Helmholtz-Zentrum Hereon, Hamburg, Germany*

(Manuscript received 25 June 2021, in final form 27 October 2021)

ABSTRACT: Two regional climate models (RCMs) participating in the CORDEX–Coordinated Output for Regional Evaluations (CORDEX-CORE) project feature a dipole-type rainfall bias during March–May (MAM) and September–November (SON) over central equatorial Africa (CEA), consisting of positive bias in west central equatorial Africa (WCEA) and negative bias in east central equatorial Africa (ECEA). One is the Regional Model version 2015 (REMO2015) and the other is the fourth version of the Regional Climate Model (RegCM4-v7). RCMs are nested in three Earth system models (ESMs) from phase 5 of the Coupled Model Intercomparison Project (CMIP5), and in the reanalysis ERA-Interim, at ~25-km spacing grid resolution. This study highlights misrepresented underlying physical processes associated with these rainfall biases through a process-based evaluation. Both RCMs produce a weaker Congo basin cell, associated with a weaker land–ocean zonal surface pressure gradient. Consequently, less water vapor enters the region, and little is transported from WCEA to ECEA, resulting in higher moisture availability in the west than in the east. This leads to an unevenly distributed moisture across the region, favoring a stronger atmospheric instability in WCEA where the moist static energy (MSE) anomalously increases through an enhanced latent static energy (LSE). Moisture arrives at a slower pace in ECEA, associated with the weak cell's strength. The intensity of ascent motions in response to the orographic constraint is weak to destabilize atmospheric stability in the lower layers, necessary for initiating deep convection. Therefore, the convection is shallow in ECEA related to underestimating the MSE due to the reduced LSE.

KEYWORDS: Atmospheric circulation; Hadley circulation; Walker circulation Atmosphere-land interaction; Water vapor; Surface pressure; Rainfall; Model evaluation/performance

## 1. Introduction

The region of central equatorial Africa (CEA) is home to the Congo rain forest, the world's second-largest, which actively absorbs carbon dioxide ($CO_2$) and modulates the global climate system (Baccini et al. 2012; Dargie et al. 2017). Its dense forest is highly sensitive to climate variability and change (Zhou et al. 2014; Bell et al. 2015; Malhi 2018; Garcin et al. 2018; Jiang et al. 2019), and the region is expected to experience the highest level of warming worldwide (King and Harrington 2018; Weber et al. 2018; Fotso-Nguemo et al. 2021). However, climate models feature large ranges of uncertainties in this domain. Even in the new generation of regional climate models (RCMs; Dosio et al. 2021a; Sørland et al. 2021; Ilori and Balogun 2021) participating in the CORDEX-CORE project (Coordinated Regional Climate Downscaling Experiment–Coordinated Output for Regional Evaluations; Giorgi et al. 2009; Jones et al. 2011; Gutowski et al. 2016), significant precipitation biases persist. As part of the CORDEX-CORE project, the capability of these RCMs must be thoroughly assessed to 1) improve existing RCMs, 2) deepen our understanding of regional precipitation drivers, which is required for model physical and dynamical formulations, and 3) ensure the accuracy of projected climate change information forwarded to decision-makers.

Tamoffo's ORCID: 0000-0001-8482-8881.

Amekudzi's ORCID: 0000-0002-2186-3425.

Weber's ORCID: 0000-0002-8133-8622.

Vondou's ORCID: 0000-0002-8681-5328.

Yamba's ORCID: 0000-0002-0486-9921.

Jacob's ORCID: 0000-0002-5249-4044.

Supplemental information related to this paper is available at the Journals Online website: https://doi.org/10.1175/JCLI-D-21-0487.s1.

*Corresponding author*: Alain T. Tamoffo, alaintamoffotchio@gmail.com

DOI: 10.1175/JCLI-D-21-0487.1

Climate modeling studies over CEA have progressed considerably in recent years despite the complexity of the area's hydrological cycle, the diversity of local and remote physical processes, mechanisms that drive the region's climate system, and the lack of reliable observational data needed to efficiently constraint model outputs (Rowell 2013; Washington et al. 2013). Numerous studies, particularly on model evaluation, have shifted away from the traditional performance-based approach (Gleckler et al. 2008) to a process-oriented approach (James et al. 2018). This is because the performance-based method simply compares the model's statistical metric to observational measures without identifying the sources of the model's inaccuracy and providing guidance for improvement. However, the process-based approach additionally determines if the simulated climatology of a diagnostic variable is linked to regional climate system factors, which affects a model's credibility in simulating current or future climatology.

According to studies using a process-based approach, the pattern of the CEA's rainfall in coupled models participating in phase 5 of the Coupled Model Intercomparison Project (CMIP5; Taylor et al. 2012) is as a result of a number of local, regional, and large-scale processes. For instance, the way models describe moisture convergence and divergence is directly linked to their rainfall climatologies (Washington et al. 2013; Creese and Washington 2016; Hua et al. 2019; Tamoffo et al. 2019). Pokam et al. (2012) highlighted the relationship between the spatiotemporal variability of the moisture convergence and that of the northern branch of the African easterly jet (AEJ-N) during March–May. The link between the September–November rainfall maximum and the southern component of the AEJ (AEJ-S), which enhances mesoscale convective systems (MCSs), was proven by Jackson et al. (2009). Large differences in the spatial distribution of CMIP5 rainfall between the western and eastern CEA were identified by Creese and Washington (2016), which were linked to a chain of drivers such as the South Atlantic high pressure system, strengthened low-level westerlies, sea surface temperature (SST) anomalies, enhanced coastal evaporation, and strengthened or weakened Walker-like circulation (Pokam et al. 2014; Creese and Washington 2018; Zhao and Cook 2021). Longandjo and Rouault (2020) recently proposed the presence of the Congo basin cell in the region throughout the year, set up by the land–ocean thermal contrast between the warm central African landmass and the cold eastern equatorial Atlantic Ocean, inducing moisture convergence. The Indian Ocean also contributes to the region's supply of water vapor (Dyer et al. 2017). The largest source of water vapor from the Indian Ocean to central Africa would be nocturnal low-level jets (LLJs) emanating from the East African Rift Valley system (Munday et al. 2021). The model's capacity to capture this process, however, is dependent on its ability to correctly reflect the topography, with higher results obtained when the horizontal resolution is ≤60 km, as they reported.

Despite the fact that the process-based methodology can effectively expose the sources of model errors, previous research has mainly relied on ESM simulations. ESMs have a lower horizontal resolution and are hence subject to a number of drawbacks. Munday et al. (2021), for instance, showed that coarse-resolution CMIP5 rainfall biases across the continent are linked to their misrepresentation of LLJs. The trustworthiness of climate information produced from CMIP5 ESMs would be severely harmed as a result of a poor representation of orographic forcings. Raghavendra (2020, see chapter 5 therein) demonstrated that orography regulates the beginning of convection subsequent development into MCSs using a high-resolution convection-permitting simulation over the Congo. As a result, reducing the spacing grid resolution of ESMs appears to be a promising solution. The downscaling is intended to improve the representation of smaller-scale physiographic processes while also adding local topographical information (Moufouma-Okia and Jones 2015; Giorgi and Gutowski 2015; Vondou and Haensler 2017). However, systematic differences between results from RCMs and observations may not necessarily be smaller than those for ESMs. Added values do not always arise from the improvement of regional processes (Tamoffo et al. 2020).

Even though several studies (e.g., Haensler et al. 2013; Dosio and Panitz 2016; Weber et al. 2017; Fotso-Nguemo et al. 2017; Taguela et al. 2020) have used downscaling to mimic the African climate and found significant enhanced utility when compared to conventional ESMs, the majority of these studies were merely descriptive and did not investigate the causes of RCM biases. Little is known about the mechanisms in RCMs that lead to underperformance in CORDEX-CORE simulations, yet their outputs will be used to drive impact models, which will help prepare the upcoming IPCC reports; this is a crucial knowledge gap for trust in their projections.

In light of these considerations, the current study analyzes rainfall biases in CEA using simulations from two CORDEX-CORE RCMs and the process-based evaluation technique. The goal of the research is to highlight misleading mechanisms in models that lead to errors in rainfall climatology. We hope that by doing so, we can encourage the improvement of these RCM performances so that they can more accurately simulate the current and future climate systems of the region, thereby improving the quality of climate data that will guide disaster preparedness, adaptation planning, and mitigation strategies. The next section (section 2) describes models, reanalysis, satellite, and gauge-based data used throughout the paper, the rainfall climatology is presented in section 3, and the land–atmosphere–ocean feedbacks are examined in section 4. In section 5, we look at how models of rainfall biases and atmospheric dynamics interact. Section 6 looks at how local convections react to atmospheric circulations, and section 7 wraps up and examines the findings.

## 2. Data and methods

### *a. Data*

Outputs of two CORDEX-CORE RCMs were used in this study. One is the Regional Model version 2015 (REMO2015; Jacob and Podzun 1997; Jacob 2001), developed at the Max Planck Institute for Meteorology in Hamburg, Germany, and

currently maintained at the Climate Service Center Germany (GERICS) in Hamburg. Details of the original model setup, based on the ECHAM4.5 ESMs, are provided in Roeckner et al. (1996), and the most recent updates can be read in Remedio et al. (2019). The other is the fourth generation of the Regional Climate Model (RegCM4-v7), originally developed at the National Center for Atmospheric Research (NCAR; Dickinson et al. 1989; Giorgi 1989), and is currently maintained in the Earth System Physics (ESP) section of the International Centre for Theoretical Physics (ICTP; Giorgi et al. 2012). The two models were chosen for analyses in this work, based on the availability of the entire column atmospheric data necessary for the diagnostic evaluation.

These hydrostatic dynamical core versions are run over the CORDEX-Africa domain (AFR-22) at 0.22° × 0.22° and over 27 vertical layers for REMO2015 and 23 for RegCM4-v7, following the configurations described in Table S1 in the online supplemental material, and using two forcing modes: the quasi-perfect forcing mode and the imperfect forcing mode. The term "quasi-perfect forcing mode" or the "evaluation/control simulation" here refers to the fact that the reanalysis data [the European Centre for Medium-Range Weather Forecasts (ECMWF) ERA-Interim data; further details are provided in Table 1] are supposed to provide relative real boundary conditions because they are obtained by data assimilation from in situ observations using a reanalysis model. However, over central Africa, measuring stations are rare and very scattered. Therefore, over areas where in situ data are missing, reanalysis results tend to be mainly influenced by the reanalysis model (Washington et al. 2013). The purpose of the "evaluation" experiment is to distinguish systematic biases (RCM internal errors) from those transmitted from large-scale boundary forcing. This mode was integrated from January 1981 through December 2010 (Remedio et al. 2019). The second set is an imperfect forcing mode, with boundary conditions from three CMIP5 (HadGEM2-ES, MPI-ESM-LR/MR, and NCC-NorESM1; for more details see Table 2). The term "imperfect forcing mode" here refers to the fact the boundary conditions are extracted from simulations (ESMs), which are themselves the approximations of the Earth system climate by means of climate models. This mode aims to highlight the RCM sensitivity responses to different large-scale atmospheric forcings. These historical simulations were performed from 1970 to 2005 (Teichmann et al. 2020).

Numerous observational, satellite-derived, and reanalysis products have been included in analyses (institutional, spacing grid resolution, and reference information are provided in Table 1). This is because the observed data display discrepancies across the CEA (Washington et al. 2013; Dosio et al. 2021b), coupled with the fact that satellite algorithms and the reanalysis model physics are different. Therefore, using multiple sources of observational data might help get an insight into the state-of-the-art regional rainfall climatology, as well as account for uncertainties between products.

For all datasets, variables utilized include precipitation, SSTs, mean sea level pressure (MSLP), evaporation, zonal and meridional wind ($u$, $v$), the vertical velocity ($\omega$), the specific humidity ($q$), surface pressure (sp), air temperature (ta), and geopotential height ($z$), all at a monthly time step and spanning from 1980 to 2005, except ARC2 and CHIRPS2 precipitation available on a daily basis, and for which the analysis periods are 1983–2005 and 1981–2005, respectively.

### b. Methods

The CEA (10°N–10°S; 10°–35°E, red boxes; Fig. 1) climatology consists of two wet seasons from March to May (MAM) and from September to November (SON), and two dry seasons from December to February (DJF) and from June to August (JJA). In this study, the focus is on the wet seasons, which encompass the majority of mechanisms driving the region's climate system. The ability of the RCMs to represent the observed spatial patterns and seasonality of rainfall was first assessed. This made it possible to subdivide the study area into western CEA (WCEA; black box in the fourth panel, Fig. 1) and eastern CEA (ECEA; black box in the fifth panel, Fig. 1), based on the spatial pattern of rainfall biases. To understand the reasons behind RCMs' biases, we use a number of better-known drivers to assess the models. These include land–sea interactions through SST, MSLP, and surface pressure variabilities (Dezfuli and Nicholson 2013; Nicholson and Dezfuli 2013); regional atmospheric circulations such as low-level westerlies (Pokam et al. 2014), the Congo basin cell (Longandjo and Rouault 2020), the Hadley-like circulation (Stachnik and Schumacher 2011), dynamics of midtropospheric jets (Nicholson and Dezfuli 2013; Kuete et al. 2019), moisture transport (Pokam et al. 2012; Dyer et al. 2017; Hua et al. 2019), and vertical motions (e.g., convection; Dezfuli et al. 2015; Cook and Vizy 2016). The methods used for estimating the regional moisture convergence/divergence, the Congo low-level cell, and the Hadley-like circulation are documented in the appendices.

## 3. Model outputs of rainfall and selection of regions of quantitative analyses

We first highlight similarities and differences (biases) in rainfall seasonal patterns between reanalysis (since they are used to diagnose the circulation fields) and RCM data as seen in Fig. 1. The remapped ARC2 combined product is used as a reference owing to its closer native resolution (0.10°) to that of simulations (0.22°), as well as to minimize errors from the interpolation process. Note that there is an agreement between ARC2 and other observational/combined measures of the region's climatology (see Figs. S1a, S2a, and S3 in the online supplemental material). In addition, similar models' structural bias is obtained when GPCC-v8 and CHIRPS2 are used as reference data (not shown).

In MAM (Fig. 1a), reanalysis products generally model higher rainfall over major parts of the region. ERA5 shows the weakest biases, with positive rainfall biases prevalent in most parts of the region. MERRA-2 features the strongest positive rainfall biases along the western, southern, and eastern borders of the CEA, and negative rainfall biases along the northern edge. Apart from the negative precipitation biases located from the center to the northern edge of the region,

TABLE 1. Description of reanalysis and satellite/gauge datasets employed for the evaluation in this study.

| Dataset | Institution | Horizontal resolution | Periods used | Reference |
|---|---|---|---|---|
| CRU-TS4.04 | Center for Atmospheric Research (NCAR) Climate Research Unit, University of East Anglia | 0.5° × 0.5° | 1980–2005 | Harris et al. (2020) |
| GPCC-v8 | Global Precipitation Climatology Centre | 0.5° × 0.5° | 1980–2005 | Schneider et al. (2013) |
| Udel-v4.01 | University of Delaware data | 0.5° × 0.5° | 1980–2005 | Legates and Willmott (1990) |
| NIC131 | New rainfall datasets recently developed for equatorial Africa | 2.5° × 2.5° | 1980–2005 | Nicholson et al. (2019) |
| CHIRPS2 | Climate Hazards Infrared Precipitation with Stations | 0.05° × 0.05° | 1981–2005 | Funk et al. (2015) |
| UGDP | Unified Gauge-Based Analysis of Global Daily Precipitation | 0.5° × 0.5° | 1980–2005 | Janowiak and Xie (2011) |
| GPCP-v3.2 | Global Precipitation Climatology Project World Climate Research Programme (WCRP) | 2.5° × 2.5° | 1980–2005 | Huffman et al. (2009) |
| ARC2 | African Rainfall Climatology, version 2 | 0.1° × 0.1° | 1983–2005 | Novella and Thiaw (2013) |
| ERA5/ERA-Interim | European Centre for Medium-Range Weather Forecasts | 0.25° × 0.25° | 1980–2005 | Hersbach et al. (2020)/ Dee et al. (2011) |
| MERRA-2 | The Modern-Era Retrospective Analysis for Research and Application, version 2 | 0.5° × 0.66° | 1980–2005 | NASA (2016) |
| NCEP2 | National Centers for Environmental Prediction (NCEP) and the National Center for Atmospheric Research (NCAR) | 2.5° × 2.5° | 1980–2005 | Kanamitsu et al. (2010) |
| HadISST2 | Met Office Hadley Centre | 1.0° × 1.0° | 1980–2005 | Titchner and Rayner (2014) |
| ERSST-v5 | NOAA National Centers for Environmental Information | 2.0° × 2.0° | 1980–2005 | Huang et al. (2017) |

NCEP2 shows positive precipitation biases elsewhere. Experiments of both REMO and RegCM4 display quasi-similar spatial polarity of biases. They feature wet biases in the major part of WCEA and dry biases in ECEA.

In SON (Fig. 1b), ERA5 presents quasi-homogeneous positive rainfall biases. MERRA-2 features strong wet biases throughout the western and eastern frontiers, but moderate dry biases in the center and along the northern and southern borders. NCEP2 simulates strong wet biases in most parts of the region and dry biases in a small portion of the northwestern sector. Experiments always feature the bipolar character of rainfall bias patterns as in MAM season, but with some differences. For instance, REMO-ERA shows lower biases in SON than in MAM. RegCM4-ERA features dry biases in coastal areas and wet biases in the interior of WCEA. Runs resulting from the imperfect forcing mode intensify wet biases, which propagate farther toward the eastern border in SON than in MAM.

It is worth noting that the differences in the rainfall climatology among reanalysis data over CEA are associated with their differences in simulating the lower and midlayer tropospheric circulation (Hua et al. 2019). By comparing control

TABLE 2. Details of driving ESMs and names of RCM experiments used in this study.

| Institution | ESMs | RCMs (0.22° × 0.22°) | Run names | Periods used | Reference |
|---|---|---|---|---|---|
| Met Office Hadley Centre | HadGEM2-ES (1.25° × 1.875°) | REMO2015<br>RegCM4-v7 | REMO-HadGEM2<br>RegCM4-HadGEM2 | 1980–2005 | Collins et al. (2011) |
| Max Planck Institute for Meteorology | MPI-ESM-LR/ MPI-ESM-MR (1.865° × 1.875°) | REMO2015<br>RegCM4-v7 | REMO-MPI-LR<br>RegCM4-MPI-MR | 1980–2005 | Popke et al. (2013)/ Stevens et al. (2013) |
| Norwegian Climate Center | NCC-NorESM (1.894° × 2.5°) | REMO2015<br>RegCM4-v7 | REMO-NorESM1<br>RegCM4-NorESM1 | 1980–2005 | Bentsen et al. (2013) |

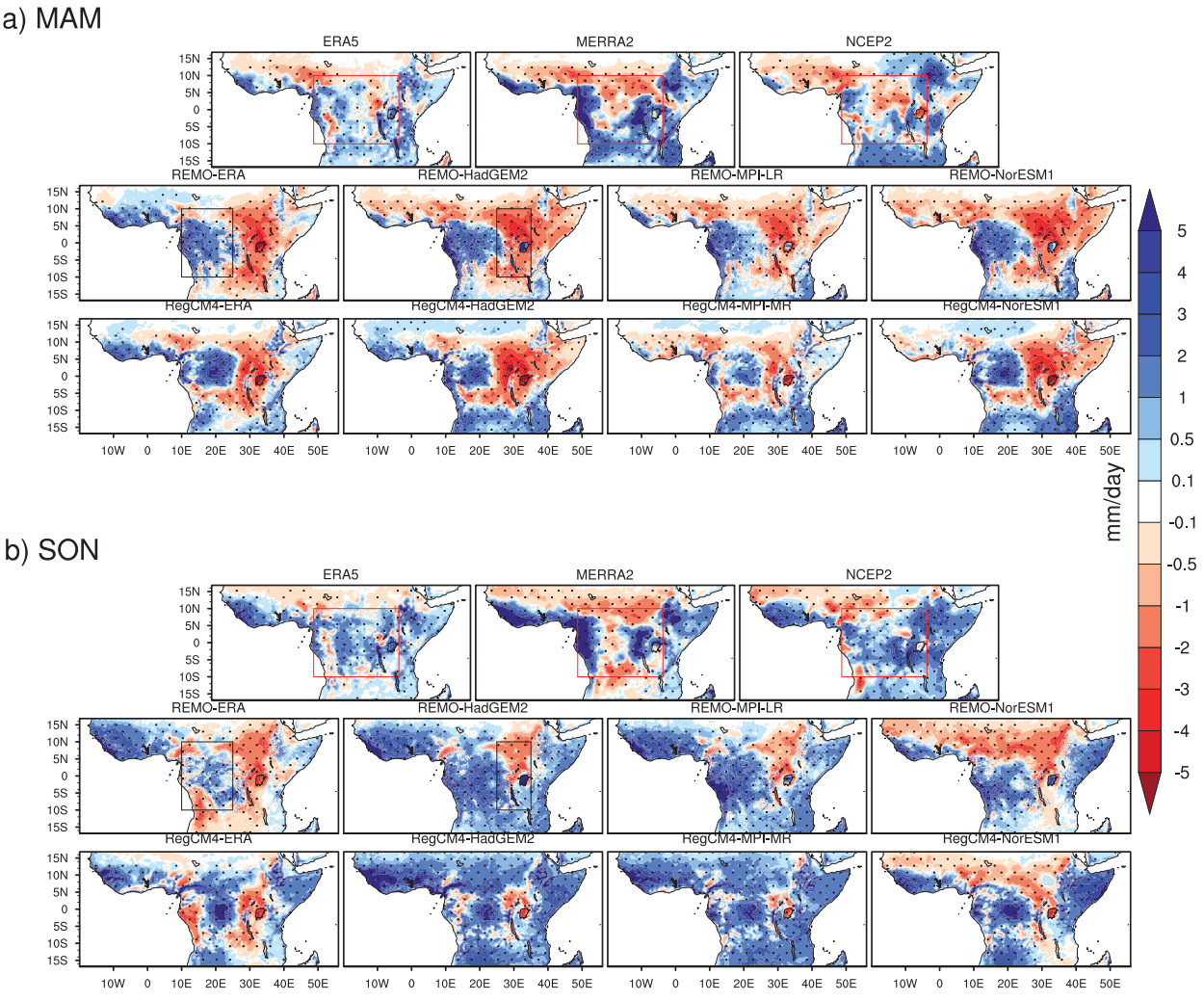


FIG. 1. Long-term mean (1983–2005) rainfall biases (RCM-runs/reanalysis data minus ARC2; mm day$^{-1}$), for the (a) MAM and (b) SON seasons. The ARC2 dataset is used as a point of reference to assess the two RCM experiment (REMO2015 and RegCM4-v7) and reanalysis product biases. The stippling highlights the grid points where the rainfall bias of the dataset under consideration is statistically significant at the 95% confidence level using the Student's *t* test. Here the CEA (red boxes) is split into the WCEA (10°–25°E, 10°S–10°N; with wet biases; black box in the fourth panel) and the ECEA (25°–35°E; 10°S–10°N; with dry biases; black box in the fifth panel).

simulations with imperfect runs, it emerges that the RCMs' internal physics strongly influences the transmitted boundary conditions from ESMs. For instance, for the two RCMs, the control runs REMO-ERA and RegCM4-ERA represent a spatial structure of biases similar to those of imperfect forcings (combination RCM–ESMs). This implies that RCM biases are mainly systematic. However, the effects of boundary conditions from ESMs still exist but are less important because they only influence the magnitude of biases. For instance, in SON, the control simulation REMO-ERA shows weak wet biases in WCEA and strong dry biases in ECEA. At the same time, imperfect experiments from the same RCM have strong wet biases in WCEA and reduce the area of dry biases in ECEA considerably. Therefore, control and imperfect runs are treated in the same way in the rest of analyses.

Based on these spatial configurations of rainfall biases, we subdivided the region into WCEA (10°–25°E, 10°S–10°N) and ECEA (25°–35°E, 10°S–10°N). In WCEA, overall simulations and reanalyses capture well the bimodal distribution mode of rainfall with peaks in MAM and SON but show important intensity differences (Fig. S1b). REMO-ERA and RegCM4-ERA shift the MAM rainfall peak to March, rather than April as usual, but the overall runs agree on the SON rainfall peak observed in October. The spreads between the wettest and the driest experiments are respectively 2.5 mm day$^{-1}$ in MAM and 3 mm day$^{-1}$ in SON. Moreover, runs exhibit a strong inconsistency in the latitudinal spread of the rainband (Figs. 2a,c). For instance, the majority of experiments start the rainband north of 10°S in MAM (Fig. 2a), although they are all consistent with observations in the north. Inconsistencies occur both in north and south in SON

(Fig. 2c). Some of them overestimate the width of the rainband whereas others underestimate it. Rainfall intensity differences along latitudes between observations and model outputs are up to 3.5 mm day$^{-1}$. There are strong discrepancies with regards to the latitudinal position of rainfall peaks in the two seasons. The southernmost peak is positioned around 4°S by REMO-HadGEM2 (~9 mm day$^{-1}$) and the northernmost around 2°N by REMO-MPI-LR (~9 mm day$^{-1}$), whereas observations locate the peak around 2°S (~6 mm day$^{-1}$).

In ECEA, there are large disparities among datasets, with the spread between the wettest and the driest reaching 5 mm day$^{-1}$ during the first rainfall peak in MAM, and 3.5 mm day$^{-1}$ during the second peak in SON (Fig. S2b). Also, there is large bandwidth in the latitudinal spread of the rainband both in north and south during the two seasons (Figs. 2b,d). Here most runs shift the rainband southward both in MAM and SON seasons, with a higher rainfall amount in SON (Fig. 2b) than in MAM (Fig. 2d). Along the latitudinal migration, experiments feature stronger differences compared to observations. The driest run shows a 3 mm day$^{-1}$ rainfall deficit (within 2°–4°S by RegCM4-HadGEM2), and the wettest shows a 2 mm day$^{-1}$ rainfall surplus (within 0°–2°S by REMO-HadGEM2) during MAM. The driest run features a 2 mm day$^{-1}$ deficit (within 0°–2°S by REMO-ERA) and the wettest features a 3 mm day$^{-1}$ surplus (within 0°–2°S by REMO-HadGEM2) during SON.

Such a rainfall pattern was recently found across CMIP5 ESMs over CEA, with some models featuring peak rainfall in the western area and others in the eastern area in SON (Creese and Washington 2018). In this study, RCMs display their rainfall maxima in WCEA (overestimation) and minima in ECEA (underestimation), more markedly in MAM than in SON. Furthermore, these authors found western rainfall correlating with eastern rainfall in the months April–July, and conversely a lack of correlation during the months of August–November. They argued about the possible common processes related to rainfall in these subregions in April–July, and different mechanisms driving rainfall in August–November. In performing a similar analysis using observed and modeled rainfall (Fig. S4), it is found that, consistent with these previous findings, observed WCEA and ECEA rainfall feature a relationship in MAM ($r \geq 0.52$), but this is not the case in SON ($r \leq 0.40$), except for the ARC2 dataset ($r = 0.75$). None of the RCM experiments feature this relationship in both MAM and SON ($r \leq 0.50$). However, caution is still needed in drawing conclusions, given the recent findings of plausible mechanisms responsible for the variability of rainfall in this region (e.g., Pokam et al. 2014; Dezfuli et al. 2015; Longandjo and Rouault 2020). This is further discussed in sections 5 and 6. Likewise, strong feedbacks between both the Atlantic and Indian Oceans and the CEA's rainfall regime have been widely discussed (e.g., Wahl et al. 2009; Toniazzo and Woolnough 2013; Cook and Vizy 2016; Creese and Washington 2016; Dyer et al. 2017). To understand the reasons for RCM biases as well as their spatial polarity, we investigated how RCMs model these land–atmosphere–ocean retroactions through local SSTs and MSLPs.

## 4. Land–atmosphere–ocean feedbacks: SSTs and MSLPs

Figure 3 shows the mean climatology of MAM (Fig. 3a) and SON (Fig. 3b) SSTs over the eastern Atlantic and western Indian Oceans. It is worth noting that SSTs in RCMs are taken from corresponding driving ESMs. However, it is not necessary to show the SSTs from ESMs and RCMs. The SSTs from the ESMs would be enough. The climatological spatial distribution consists of warmer SSTs across the equatorial regions (between 10°S and 10°N) than southern oceans (south of 10°S), as shown by observations and reanalysis data from HadISST, ERA5, and ERSST. Also, MAM SSTs are generally warmer than SON ones, coherently represented by the three reference datasets. Driving ESMs seem to have strong controls on the spatial pattern of SST biases as experiments with common lateral boundary conditions feature semblable SST bias patterns. In MAM, the control experiments REMO-ERA and RegCM4-ERA show the weakest warm SST biases. Runs driven by HadGEM2 simulate strong warm SST biases along Atlantic coastlines, and cold biases both toward the interior of the Atlantic and over the whole west Indian Ocean. Downscaled experiments with MPI-ESM-LR/MR exhibit strong warm SST biases over major parts of the eastern Atlantic Ocean, while REMO-MPI-LR models strong cold biases over the western Indian Ocean. RegCM4-MPI-MR reproduces moderate cold biases over the same domain. Simulations conducted with NorESM1 display warm SST biases over areas closer to Guinea Gulf and which propagate along coastlines toward the south; however, cold SST biases are recorded in most parts of the southern Atlantic Ocean. At the same time, almost the western Indian Ocean features cold SST biases.

In SON, the two "evaluation" runs, REMO-ERA and RegCM4-ERA, also reproduce the weakest warm biases. The two RCM-HadGEM2 runs extend more warm biases over the Atlantic Ocean than in MAM, thus reducing areas of cold biases. Likewise, they model warm biases north of the western Indian Ocean and cold biases in the south. Experiments driven by MPI-ESM-LR/MR reproduce similar bias patterns observed in MAM with a slight extension of areas of cold biases in the Atlantic Ocean and rather warm biases in the Indian Ocean. In contrast, downscaled runs using NorESM1 as boundary conditions do the same, but with a slight reduction of areas of cold biases over the Atlantic Ocean, and contrastingly a slight extension of areas of warm biases over the Indian Ocean.

The nonlinear feedback controls exercised by the Atlantic, Indian, and Pacific Ocean SSTs on African precipitation systems are known (e.g., Todd and Washington 2004; Cook and Vizy 2016; Hua et al. 2016). Coupled models from CMIP3 and CMIP5 had difficulties capturing these relationships, thus impacting their outputs of rainfall (e.g., Cook and Vizy 2006; Rowell 2013). We evaluated the performances of each RCM experiment to model these teleconnections, in computing the time series' linear correlations between regional WCEA (Fig. S5) and ECEA (Fig. S6) rainfall and both ocean SSTs. This analysis can be read in Text S1 in the online supplemental information.

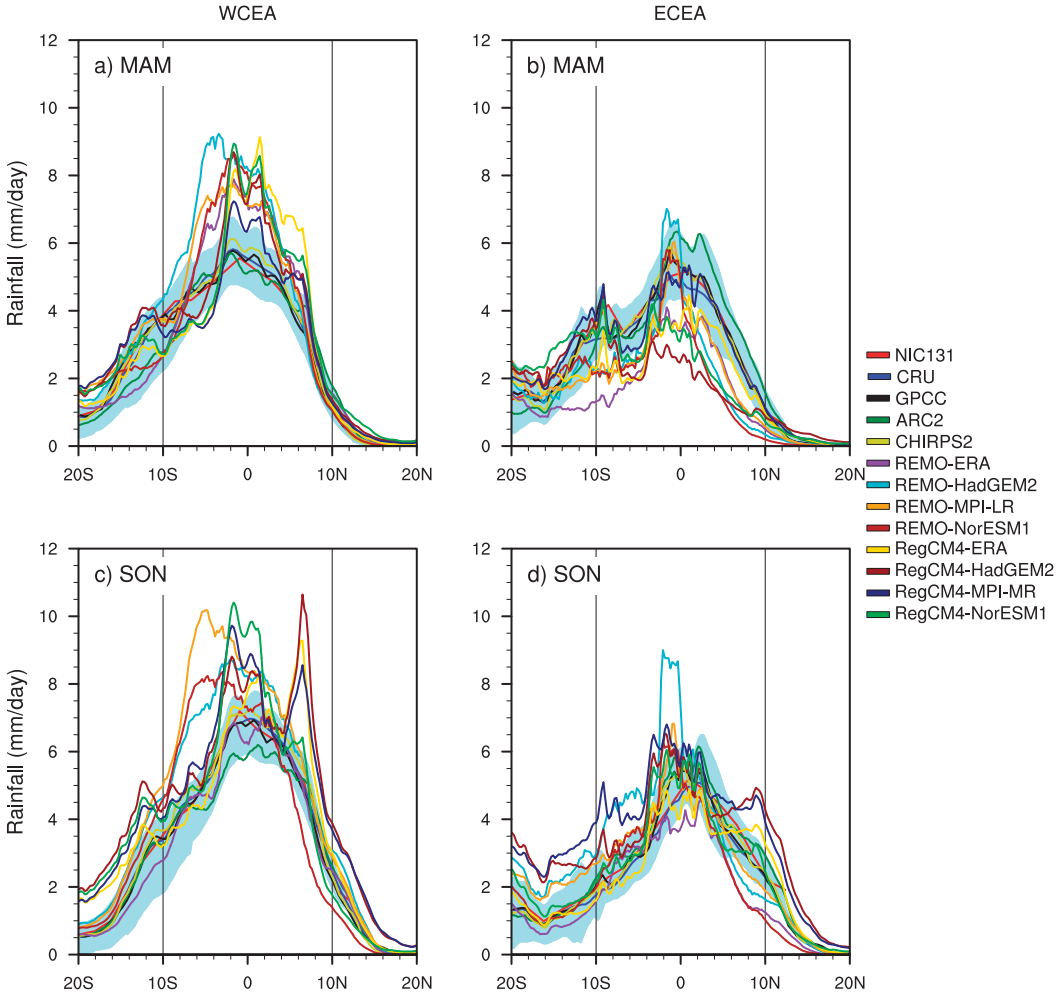


FIG. 2. Latitudinal spread of the rainband in (top) MAM and (bottom) SON over (a),(c) WCEA and (b),(d) ECEA. Data used include the rain gauge, satellite, and combined products, and from the REMO2015 and RegCM4-v7 experiments. The data cover the period 1980–2005, apart from ARC2 dataset, which covers the period 1983–2005, and the CHIRPS2 dataset, which covers the period 1981–2005. The shaded light-blue band is the standard deviation and uses the CRU, GPCC, NIC131-gridded, ARC2, and CHIRPS2 ensemble mean, from 1983 to 2005. An experiment out of the standard deviation band is considered to have failed to simulate the latitudinal migration of the rainband.

The complexity of the relationship between SSTs and CEA rainfall is known (e.g., Balas et al. 2007; Dezfuli and Nicholson 2013; Nicholson and Dezfuli 2013; Creese and Washington 2018). Owing to the limited geographical area used in dynamical downscaling, some processes resulting from these teleconnections cannot be diagnosed or can only be partly analyzed in this study, although they might be important drivers of rainfall biases, such as the tropical Walker circulation (Hua et al. 2016). Other factors not analyzed in this study may also be sources of uncertainty and model biases such as the tropical waves (e.g., Kelvin waves), the Madden–Julian oscillation (MJO), and the tropical convection (Hung et al. 2013; Sinclaire et al. 2015; Raghavendra et al. 2019). Furthermore, from Fig. 3 it emerges that simulated remote forcings (investigated in section 5) could be stronger or weaker depending on the sign and the robustness of the teleconnection. However, a direct consequence of warm SSTs is a potential increase in evaporation over oceans, which in turn could enhance advected water vapor into the region in intensifying low-level westerlies (LLWs), thereby increasing rainfall amount through the local convection. Cold SSTs would induce opposite effects (Creesse and Washington 2018). Inland positive evaporation biases would presumably accelerate the hydrological cycle in accentuating the moisture recycling process; negative evaporation biases would slow down the hydrological cycle, thus reducing the moisture availability (Pokam et al. 2012, Dyer et al. 2017). Therefore, we have investigated models of evaporation (Fig. S7) both over oceans and land, as shown in Text S2 in the online supplemental information.

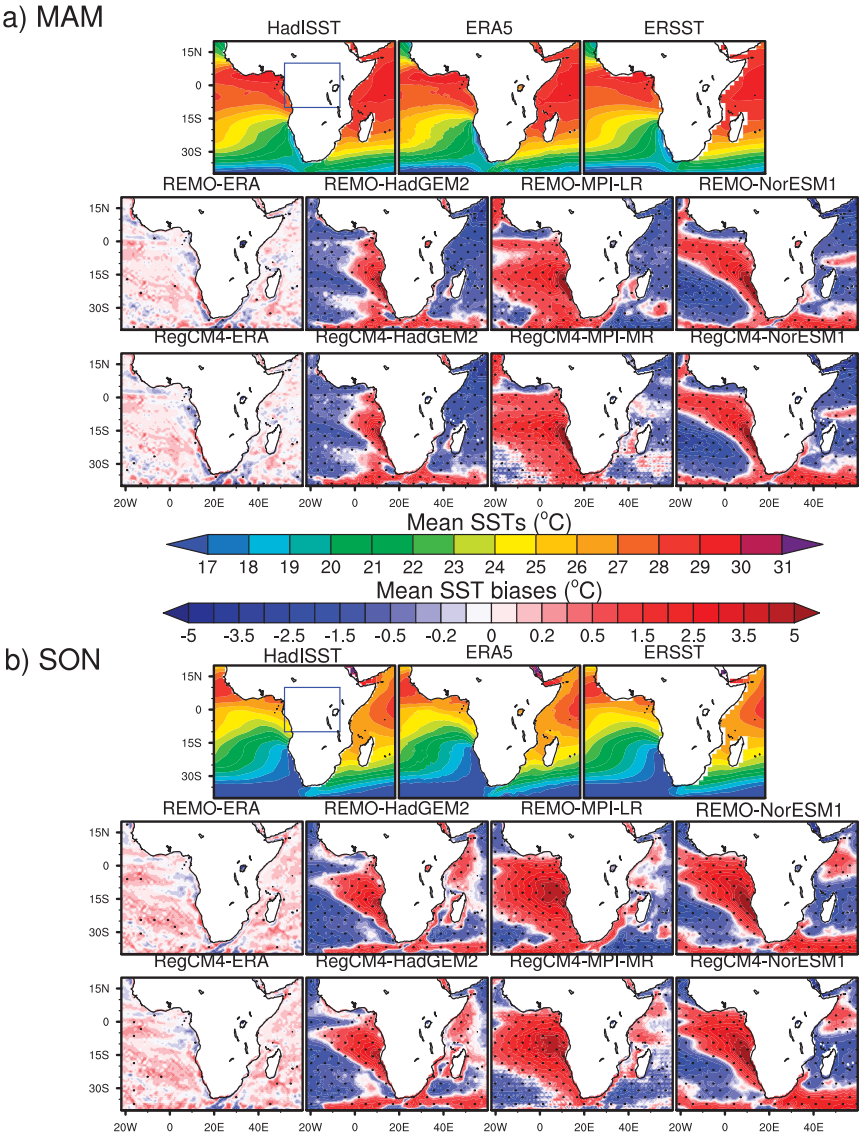


FIG. 3. Mean (1980–2005) seasonal SST climatology (in the top row) and SST biases (in the middle and bottom rows) for (a) MAM and (b) SON. The climatology is obtained from reanalysis data (HadISST, ERA5, and ERSST). The biases are computed relative to ERA5 reanalysis, from the REMO2015 and RegCM4-v7 experiments. The stippling occurs where the difference between the dataset under consideration and the ERA5 reanalysis dataset is statistically significant at the 95% confidence level by means of the Student's *t* test. The black boxes indicate the CEA.

Likewise, overall RCM runs model weaker MSLPs in the two seasons (Fig. 4). A direct impact of this underestimation is the weakening of the intensity of the tropical zonal circulation, which strongly governs the rainfall variability over CEA (Nicholson and Dezfuli 2013; Longandjo and Rouault 2020) and is also investigated in section 5. It should be noted that the relationships between rainfall and MSLP over WCEA and ECEA (not shown) are not necessarily similar to those with SST. In fact, although MSLP variations are associated with variations in SSTs, the distribution of one is not only influenced by the other parameter. So, it is not possible to have systematic bias correspondences. Other atmospheric or oceanic forcings play an important role in MSLP anomalies such as oceanic oscillations (Morioka et al. 2014). These SST and MSLP biases could have strong consequences on wind dynamics (Creese and Washington 2018), therefore prompting the analysis of simulated atmospheric circulation. The Saharan and the Angolan low pressure systems also exercise a strong control on the CEA circulation (Chen 2004; Kuete et al. 2019 ; Cook et al. 2020). Thus, we

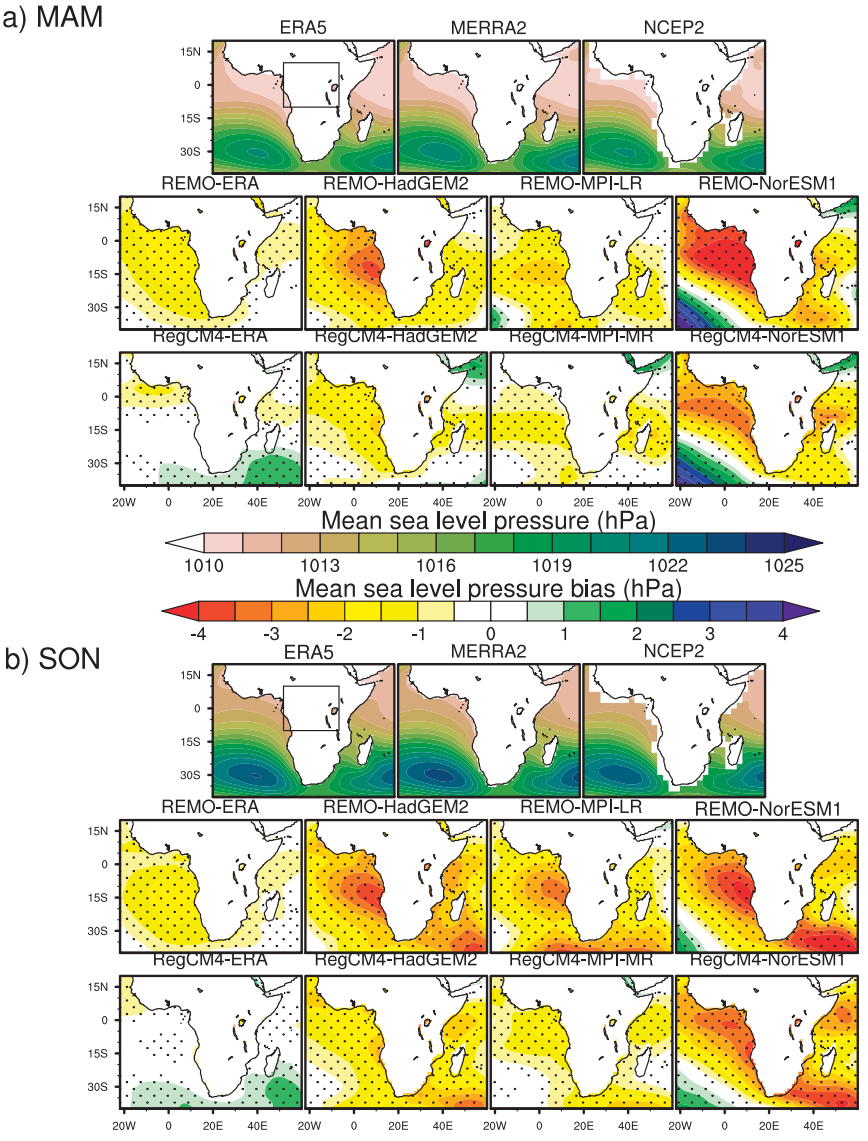


FIG. 4. Mean (1980–2005) seasonal SLP climatology (in the top row) and SLP biases (in the middle and bottom rows) for (a) MAM and (b) SON. The climatology is obtained from reanalysis data (ERA5, MERRA-2, and NCEP2). The biases are computed relative to ERA5 reanalysis, from REMO2015 and RegCM4-v7 experiments. The stippling occurs where the difference between the dataset under consideration and the ERA5 reanalysis dataset is statistically significant at the 95% confidence level by means of the Student's *t* test. The black boxes indicate the CEA.

also analyzed the RCMs of land surface pressure (sp) outputs (not shown) to outline whether model runs feature particular behaviors over these areas. Ensuing results show slight modeled weak surface pressure across all land regions, more pronounced in REMO runs than RegCM4 runs. However, none of the RCM experiments features particular aspects over the Saharan thermal low or the Angolan low. This suggests that low pressure systems did not play any major role in determining models' wetness or dryness.

## 5. Links with dynamics of atmospheric circulation

The present section aims at detecting atmospheric circulation behaviors associated with rainfall biases, and links with land–atmosphere–ocean feedback biases. The emphasis is placed on how models represent transient zonal ($Q_Z$) and meridional ($Q_m$) regional moisture across CEA, and how they affect the total column ($Q_T$) moisture convergence, as well as the moisture transport (e.g., Dyer et al. 2017; Tamoffo et al. 2021). Note that reanalysis data are used here for qualitative

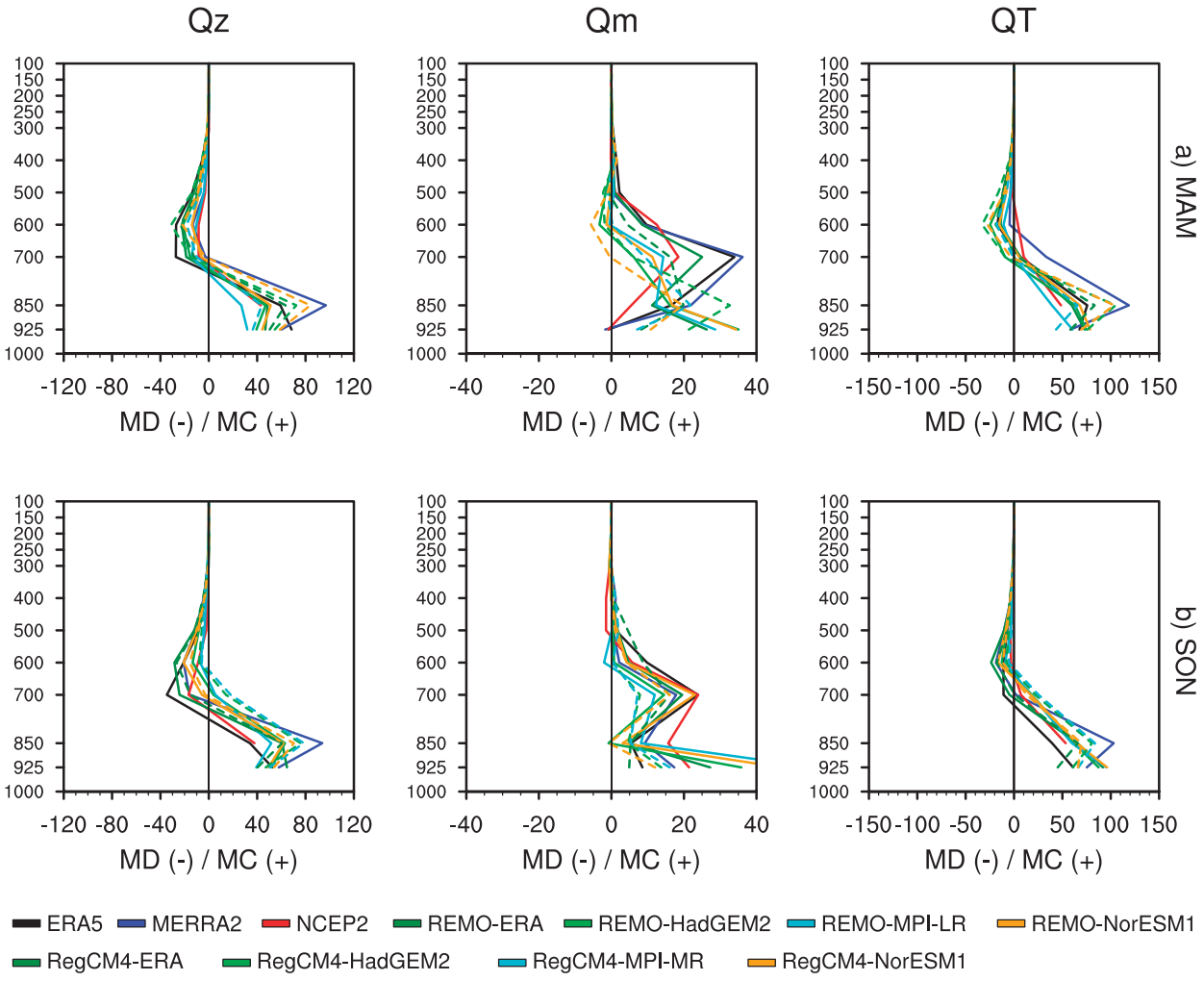


FIG. 5. Vertical profile of the regional moisture convergence/divergence (kg $m^{-1}$ $s^{-1}$) across the CEA, divided into the (left) zonal ($Q_Z$) and (center) meridional ($Q_m$) directions, in (a) MAM and (b) SON. (right) The total column moisture convergence/divergence ($Q_T$); MD = moisture divergence (negative values) and MC = moisture convergence (positive values). Data used are from reanalyses ERA5, MERRA-2, and NCEP2, and from experiments REMO2015 (solid lines) and RegCM4-v7 (dashed lines) over the period 1980–2005.

rather than quantitative purposes, as they were not used as a reference for calculating the precipitation bias of RCM experiments.

### *a. Regional moisture convergence or divergence*

The diagnostic of the vertical profile of water vapor (Fig. 5) provided insight into how RCMs model moisture transport across various pressure levels of the CEA. This helps highlight which circulation dominates the moisture supply and where the moisture surplus or deficit probably originates. Overall, the experiments feature great performances in capturing variabilities into the tropospheric column moisture content in the two directions and in both seasons, although differences in terms of intensity are obvious, which in turn bias the total moisture balance. Notably, simulations outperform in the zonal direction compared to the meridional. This alerts the state of the models of Walker- and Hadley-like circulations and is investigated in sections 5b and 5c. As demonstrated in Pokam et al. (2012), $Q_Z$ acted as the most significant contributor to the convergent peak around 850 hPa in $Q_T$, as $Q_m$ is generally weaker. Likewise, $Q_T$ is divergent in the midlayers (700–600 hPa), stronger in MAM (Fig. 5a) than in SON (Fig. 5b), resulting from the higher divergent $Q_Z$ than convergent $Q_m$. However, although model outputs of the vertical profile of moisture are promising, this does not ensure that moisture transport is properly distributed in the different layers of the troposphere across the region.

From Fig. 6, it explicitly appears that, at the bottom layers (1000–850 hPa) and in MAM (Fig. 6a), relative to reanalysis products, REMO runs produce stronger LLWs (and therefore stronger advected moisture) from the Atlantic Ocean toward the equatorial western boundary of the Congo Basin. RegCM4 runs do the least. However, the analysis of the zonal integrated moisture transport ($Q_u$) reveals underestimated and less latitudinally extended moisture into inland areas. As a consequence,

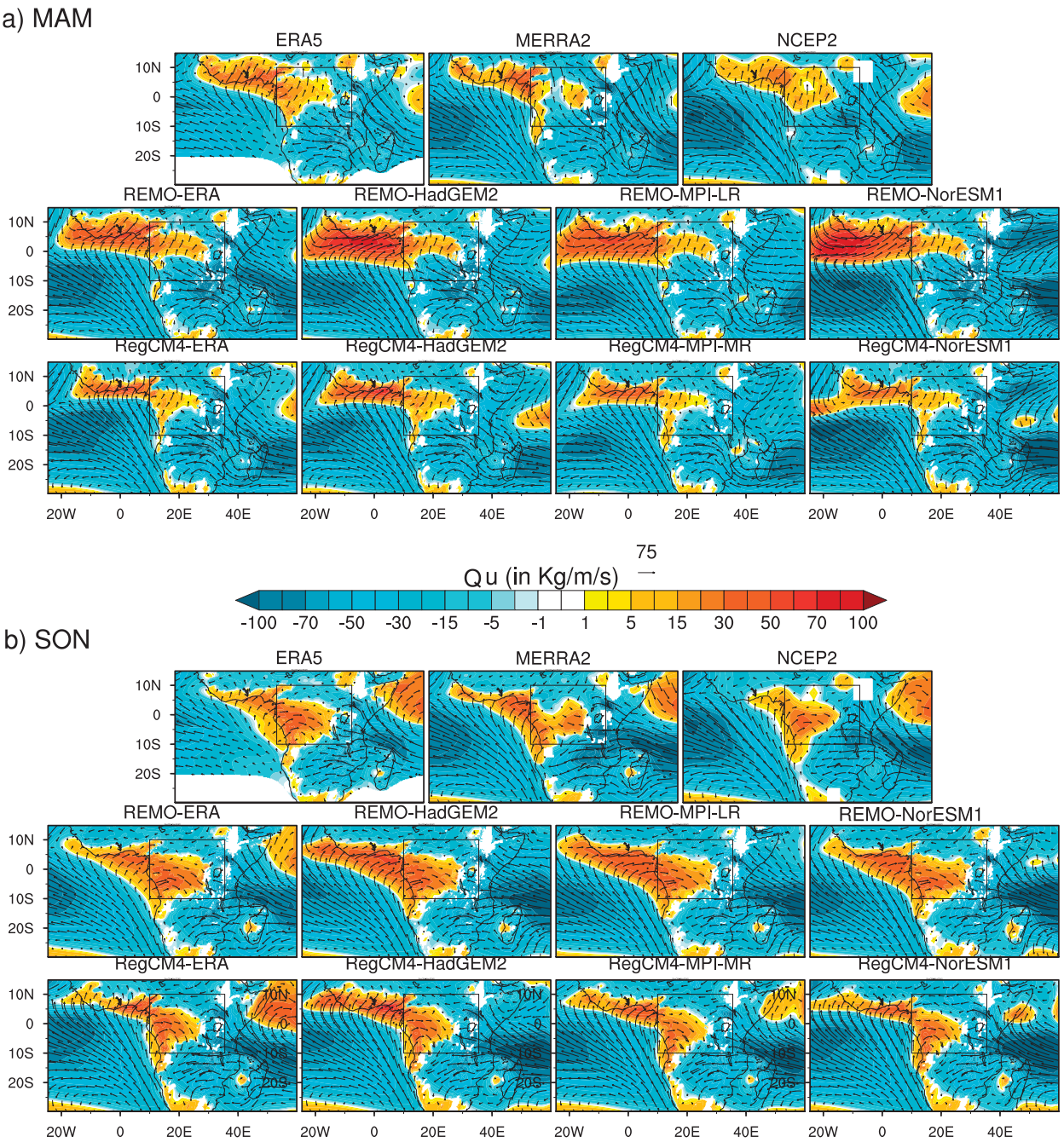


FIG. 6. Mean (1980–2005) seasonal climatology of (a) MAM and (b) SON lower-layer (1000–850 hPa) zonal vertically integrated moisture flux ($Q_u$; kg m$^{-1}$ s$^{-1}$; shaded) superimposed with vertically integrated (1000–850 hPa) total moisture transport ($Q_T$; kg m$^{-1}$ s$^{-1}$; vectors). Data used are from reanalyses (ERA5, MERRA-2, and NCEP2) and from the REMO2015 and RegCM4-v7 experiments. Negative values indicate easterly flows and positive values are westerly flows. Black boxes denote the CEA.

weaker moisture is transported from WCEA to ECEA. RCMs model stronger moisture originating from the southwest Indian Ocean. These southeasterlies recurve into southerlies while crossing the southern border and feed the WCEA, thus increasing the amount of moisture availability. The topographic forcing effect that constrains the supply of moisture originating from the Indian Ocean to central Africa in the lower troposphere through the eastern border of ECEA (Munday et al. 2021) seems well captured by all runs, as they show a good representation of transient moisture across this frontier. In SON (Fig. 6b), both the REMO and RegCM4 simulations overestimate the strengthening of LLWs. As a result, moisture transport

from the Atlantic is higher, thus increasing moisture availability both in WCEA and ECEA. These dynamic features of the moisture transport indicate that in the two seasons the moisture availability is more important in WCEA than ECEA, matching with spatial patterns of model rainfall biases.

A similar analysis performed in midlayers (700–600 hPa; not shown) shows that downscaled ESMs represent well the basic structure of midtropospheric moisture transport, but with some differences in terms of intensity of outflows at the western and inflows at the eastern borders. Given the modulator effect of AEJs on the circulation in these layers (Nicholson and Grist 2003; Jackson et al. 2009), we examined the ability of RCMs in simulating these easterlies. Figure 7 shows that in MAM (Fig. 7a), except for RegCM4-MPI-MR, the other runs correctly detect the positioning of the AEJ-N core. This is not the case in SON (Fig. 7b) where none of the RCM–ESM combinations succeeded in distinctly positioning the two cores of AEJ-N and AEJ-S. Most runs strongly underestimate the intensity of the AEJ-S component or fail to detect it neatly. Inconsistencies occur within models of AEJ intensity, with some showing weaker jet cores both in MAM and SON (e.g., RegCM4-MPI-MR) and other stronger jet cores (e.g., REMO/RegCM4-ERA, REMO/RegCM4-NorESM1). Differences in the amounts of advected moisture in these layers, particularly in MAM, are found associated with AEJ core biases because it is the time of strong moisture advection into the Congo basin via the AEJ-N, as demonstrated in Pokam et al. (2012) and Hua et al. (2019). Also, REMO/RegCM4-MPI-LR/MR, which features lower rainfall dry biases in MAM, also shows weaker AEJ-N intensity. In SON, REMO/RegCM4-NorESM1, which propagated stronger rainfall dry biases, also simulates a single, but stronger AEJ-N intensity that is more intense than both AEJ-N and AEJ-S intensities in some experiments. This corroborates previous findings by Dezfuli and Nicholson (2013), who showed that over the WCEA wet composites feature weaker midtropospheric jets than dry ones. Recently, Longandjo and Rouault (2020) demonstrated the relationship between AEJs and the low-level circulation through the Congo basin cell. They showed that the seasonality of AEJs and that of the Congo basin cell intensity, width, and its eastward extension are all controlled by the near-surface land–ocean thermal contrast, via the zonal surface pressure gradient. Also, the Congo basin cell is found to be a crucial driver of the region's precipitation system because it controls the zonal positioning of maximum rainfall. Therefore, would the presence of biases in the models of AEJs indicate biased simulations of the Congo basin cell?

### b. *The Congo basin cell*

In the preceding section, we found that although RCM runs simulate strong moisture transport over the Gulf of Guinea and coastal areas of WCEA, a smaller quantity penetrates inland to reach the highlands of eastern Ethiopia. Dezfuli et al. (2015) showed that this moisture generally rises the up-branch of the Walker-like cell over Rift Valley highlands around 33°E, then enters the mesoscale convective systems (MCSs) embedded within AEJs, which move westward and are responsible for much of the convective rainfall over the region. Figure 8 confirms that the low moisture penetration inland, especially in MAM (Fig. 8a), is associated with biases in the western and eastern edge positions, width (zonal extent), and intensity of the Congo basin cell. Except for REMO-ERA, and inconsistently with all reanalyses that show a cell starting around 2.5°E, other simulations show a cell starting from a farther west position (exceeding west of 20°W) and ending once it crosses the western border of the basin at 10°E. This is better marked in REMO experiments, as there is not the 1000-hPa pressure level available for RegCM4 simulations and which, however, would have allowed better visualization of the cell on the surface. Yet two of the three reanalysis products, namely ERA5 and NCEP2, show a cell extending to 25°E. All REMO-ESM simulations produce a wider cell, but with the western and eastern edges abnormally too westward. In terms of intensity (obtained by vertically integrating the zonal $\psi_Z$ mass-weighted streamfunction from the surface up to 850 hPa, then filtering and retaining only the negative values over the longitude band of the Congo basin), reanalysis data feature a Congo basin cell strength within the range from −14.3 (MERRA-2) to −81.7 $\times$ $10^9$ kg $s^{-1}$ (ERA5). REMO-ERA shows a cell intensity of −34.7 $\times$ $10^9$ kg $s^{-1}$, which is within the range of reanalyses, thus outperforming other simulations, and which, presumably, would be linked to good boundary conditions received from the ERA-Interim reanalysis. All REMO-ESM experiments feature a weaker Congo basin cell strength relative to the three reanalyses, with values within the range from −9.3 (REMO-NorESM1) to −14.92 $\times$ $10^9$ kg $s^{-1}$ (REMO-HadGEM2). In SON (Fig. 8b), all downscaled ESMs both from REMO and RegCM4 feature a more realistic modeled cell. For instance, consistently with the three reanalysis products, REMO runs present a cell starting around 0° that slightly crosses the longitude 25°E. Although the 1000-hPa surface pressure level is not available in RegCM4, this also seems to be the case for its runs. Experiments and reanalyses are almost coherent on the width of the cell, with the western edge included within longitudes 3°W and 3°E, and the eastern one between 25° and 27°E. The Congo basin cell strengthens in SON. Reanalyses exhibit intensity values ranging from −67.4 (MERRA-2) to −145.7 $\times$ $10^9$ kg $s^{-1}$ (ERA5). The REMO-ERA run features the strongest cell with an intensity of −194.4 $\times$ $10^9$ kg $s^{-1}$. REMO runs do so within the range from −119.0 (REMO-NorESM1) to −159.7 $\times$ $10^9$ kg $s^{-1}$ (REMO-HadGEM2). As seen in Fig. 1b, the weakening of simulated rainfall dry biases in ECEA in SON is associated with the better representation of the cell in models that, owing to the strengthening of the cell, import more moisture from the Atlantic Ocean toward inland areas than in MAM.

The aforementioned results are supported by previous findings by Longandjo and Rouault (2020) because the spatiotemporal pattern of rainfall biases corroborates well with the ones of the Congo basin cell. These authors also showed that, although there is not a direct relationship between local rainfall and the Congo basin cell, the cell nevertheless influences the zonal rainfall maximum positions. Likewise, they demonstrated that the cell is modulated by the zonal surface pressure

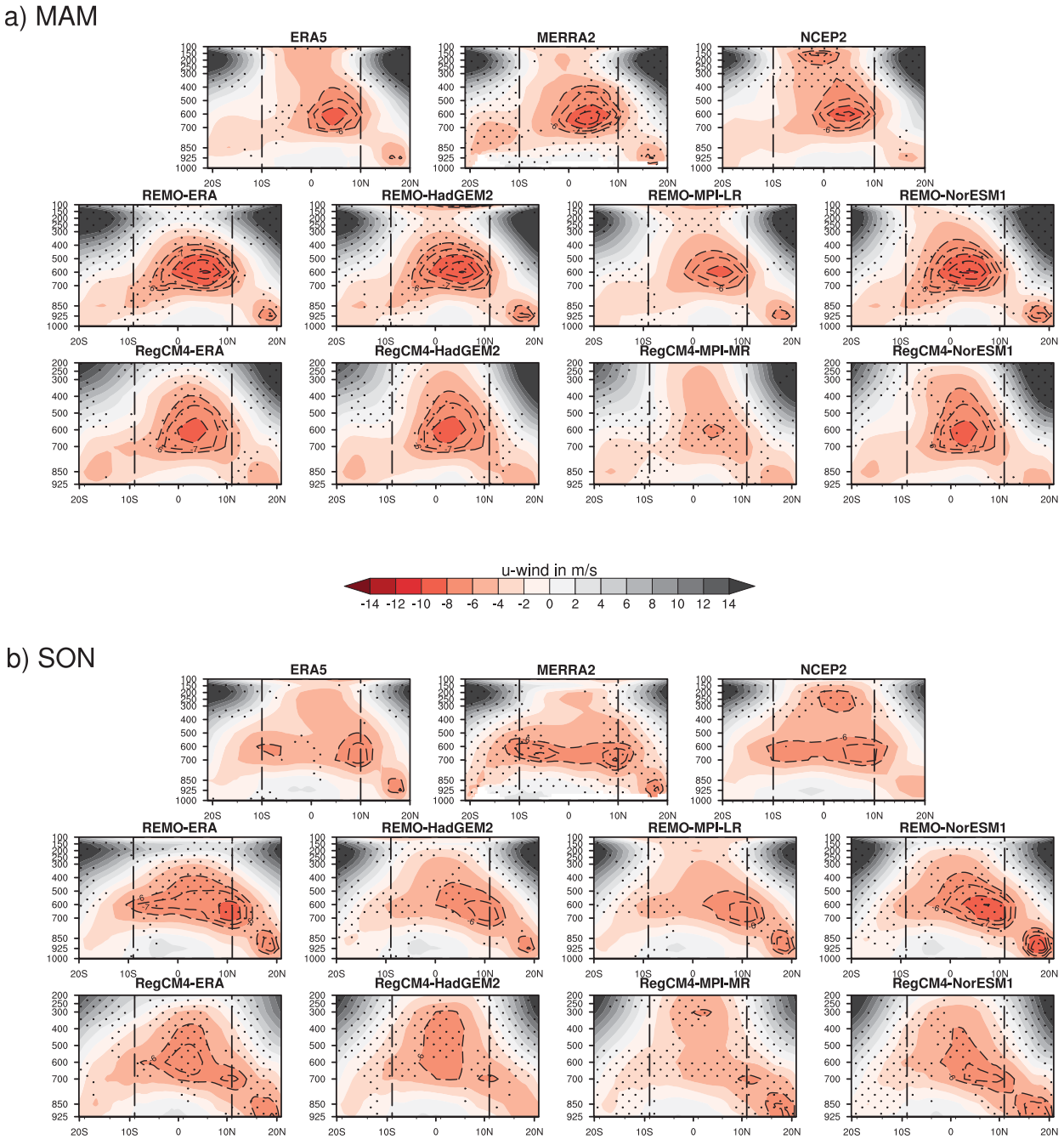


FIG. 7. Latitude–height cross sections of (a) MAM and (b) SON zonal wind ($u$ wind; m s$^{-1}$; shaded), averaged over longitudes 10°–30°E [following Nicholson and Grist (2003)]. Overlaid dashed contours indicate the mean seasonal location of AEJs (wind speed $\leq -6$ m s$^{-1}$). Data used are from the reanalyses ERA5, MERRA-2, and NCEP2 and the experiments REMO2015 and RegCM4-v7, from 1980 to 2005. The stippling occurs where the difference between the dataset under consideration and the ensemble mean of the three reanalysis products is statistically significant at the 95% confidence level by means of the Student's $t$ test. The black bars delimit the CEA latitudinal band.

gradient ($\nabla P$) via the near-surface land–ocean thermal contrast ($\nabla T$): an enhanced $\nabla T$ strengthens $\nabla P$, which in turn, intensifies the Congo basin cell and increases its width by extending more eastward the eastern edge. To understand the causality of simulated Congo basin cell biases and to assess the credibility of these mechanisms to drive the spatiotemporal patterns of modeled rainfall biases, we have also investigated simulated $\nabla T$ and $\nabla P$ as shown in Fig. 9. Although our

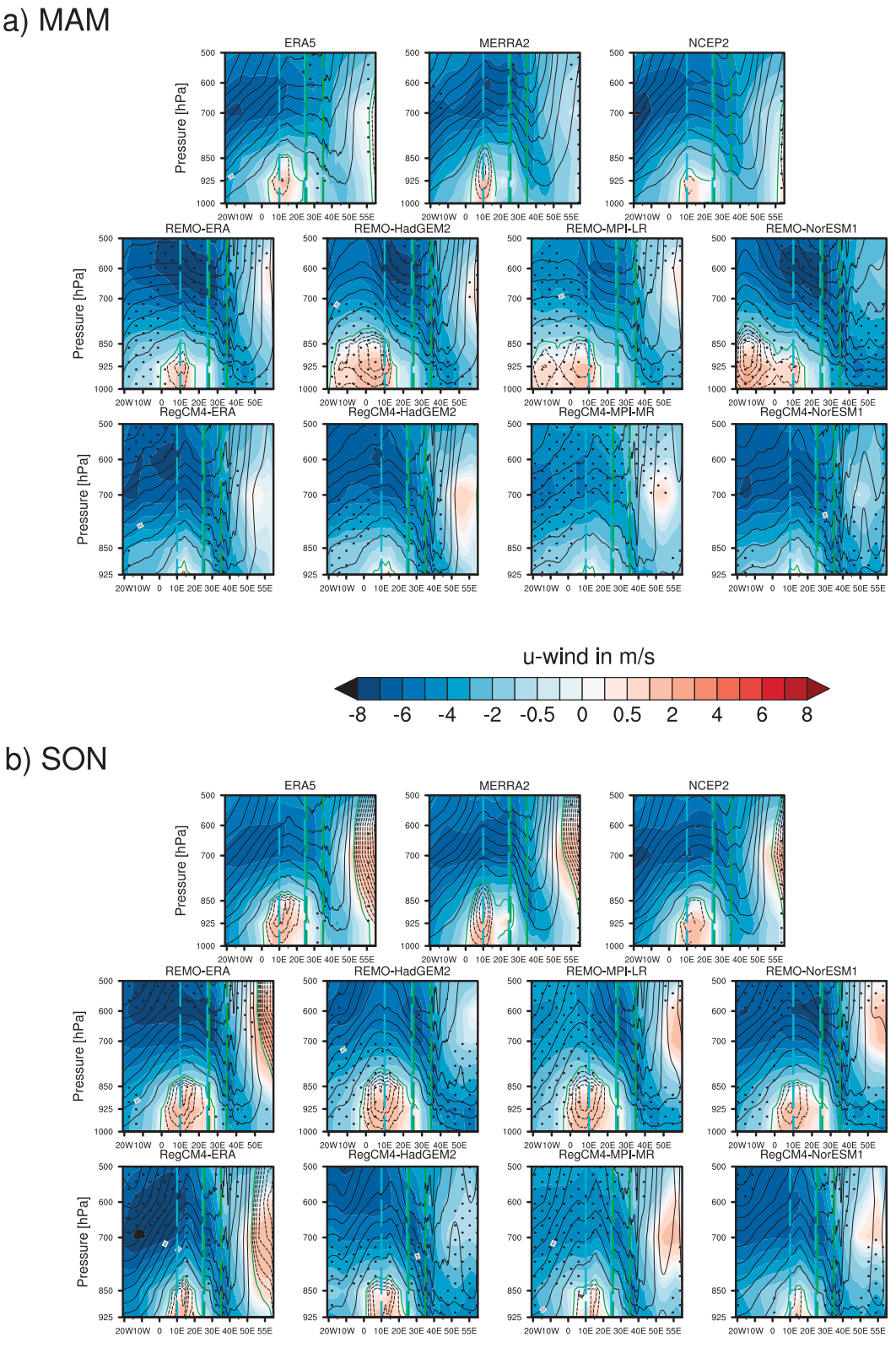


FIG. 8. Mean (1980–2005) seasonal climatology of (a) MAM and (b) SON zonal mass-weighted streamfunction ($\psi_Z$; contours in $\times 10^{11}$ kg s$^{-1}$) and mean zonal wind (shaded; m s$^{-1}$). Data used are from reanalysis data (ERA5, MERRA-2, and NCEP2) and from the REMO2015 and RegCM4-v7 experiments. Solid lines denote positive values

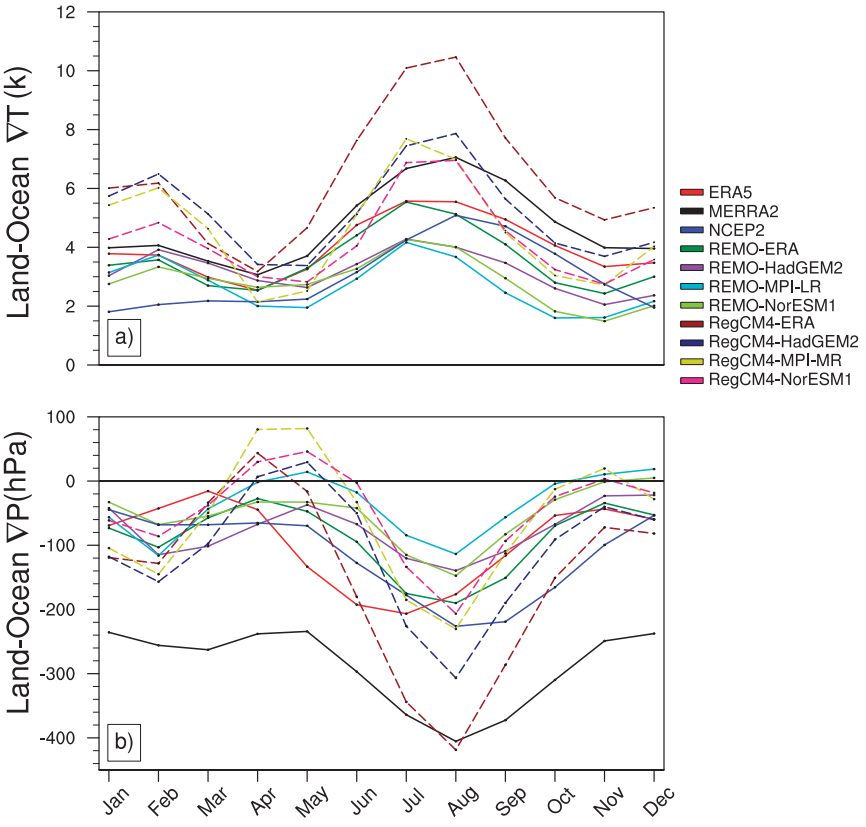


FIG. 9. Seasonality of the near-surface (a) land–ocean temperature difference (thermal contrast; $\nabla T$; K) and (b) land surface pressure and ocean sea level pressure difference ($\nabla P$; hPa) between the interior of the continent (15°–30°E, 5°S–5°N) and the equatorial eastern Atlantic Ocean (5°W–5°E, 5°S–5°N), for the ERA5, MERRA-2, and NCEP2 reanalysis data, and for the REMO2015 (solid lines) and RegCM4-v7 (dashed lines) experiments, over the period 1980–2005.

analysis is focused on seasons MAM and SON, in the first-order assessment we found that the shape of the annual cycle is common for reanalyses and model outputs both in $\nabla T$ (Fig. 9a) and $\nabla P$ (Fig. 9b). All datasets agree on months of maxima and minima in $\nabla T$. Such is not the case in $\nabla P$ between the reanalyses themselves on the one hand and between the reanalyses and the models on the other. For instance, MERRA-2 and NCEP2 place the MAM peak of $\nabla P$ in April–May, whereas ERA5 does so in March. Some RCM runs (e.g., RegCM4-MPI-MR, REMO/RegCM4-ERA) feature the MAM peak of $\nabla P$ in April–May; others (e.g., RegCM4-HadGEM2/NorESM1, REMO-MPI-LR) do so in May. Consistently with modeled weaker Congo basin cell in MAM as seen in Fig. 8a, all RCMs simulate a weaker $\nabla P$ relative to all reanalyses, with most RegCM4 runs showing rather lower MSLPs than land surface pressure. We found previously that the Congo basin cell was better simulated in SON than in MAM. Also, $\nabla T$ and $\nabla P$ are better simulated in SON than in MAM, with all datasets agreeing on months of maximum and minimum both in $\nabla T$ and $\nabla P$. Likewise, models produce a strengthened cell in SON, associated with an enhanced $\nabla P$. Therefore, $\nabla T$ and $\nabla P$ biases correlate with Congo basin cell biases, which attests to the plausibility of these mechanisms.

←

of mass-weighted streamfunctions, and dashed lines are negative values. The green line is the zero contour of the mass-weighted streamfunction ($\psi_Z = 0$) and delimits the Congo basin cell. Contour intervals are $-2 \times 10^{11}$ kg s$^{-1}$ for negative values and $10 \times 10^{11}$ kg s$^{-1}$ for positive values. The stippling highlights the grid points where the difference between the dataset under consideration and the ensemble mean of the three reanalysis products is statistically significant at the 95% confidence level using the Student's $t$ test. The cyan bars delimit the WCEA and the green ones the ECEA.

*c. The Hadley-like circulation*

To complete the diagnostic of the modeled atmospheric circulation, we also analyzed simulated Hadley-like circulation, using the meridional $\psi_M$ mass-weighted streamfunction as shown in Figs. 10 and 11. Wet biases dominate the WCEA and dry biases the ECEA. It is hypothesized that factors responsible for rainfall biases in the two areas might be different. Therefore, the analysis of the Hadley-like cell is conducted separately in the two regions.

In WCEA (Fig. 10) and in MAM (Fig. 10a), the three reanalysis datasets agree on the pattern of the cell, consisting of an ascending branch entering the basin through the southern latitudes that is wide in the lower troposphere but progressively narrower toward the upper layers. The northern descending component occupies a part of the basin in the upper troposphere, then exits from 700 to 925 hPa, where it recurves into northerlies. The southern sinking branch is far from the basin. Slightly larger in the upper troposphere, it progressively shrinks while moving toward lower layers until 700 hPa, where it recurves into southerlies. REMO experiments capture well the basic structure of the Hadley circulation, although they strongly narrow the band of the ascending branch (REMO-ESMs). Two of them, REMO-ERA and REMO-NorESM1, which simulate a stronger rising branch, simulate a stronger southern descending component but rather a weaker northern sinking one. The other two, REMO-HadGEM2 and REMO-MPI-LR, produce weaker values in major parts of the cell. RegCM4 runs feature the weakest performance in representing the cell: they strongly underestimate the ascending branch, overestimate the southern sinking branch, and completely fail to reproduce the northern descending branch. In SON (Fig. 10b), reanalyses show that the upward component weakens and moves farther outward from the basin through the southern latitudes. At the same time, the northern downward component intensifies, and the southern one limits around 600 hPa (ERA5 and NCEP2) and 300 hPa (MERRA-2). REMO simulations fail in capturing the SON Hadley-type circulation: they strongly underestimate the part of the ascending branch inside the region. Some of them (e.g., REMO-ERA and REMO-NorESM1) better capture the two sinking branches, whereas others (e.g., REMO-HadGEM2 and REMO-MPI-LR) underestimate them. Even RegCM4 simulations model a weaker upward branch including the part outside the basin. They feature a better captured southern downward component than northern one.

In ECEA (Fig. 11) and in MAM (Fig. 11a), the rising component penetrates the domain between 925 and 500 hPa for ERA5, from 925 hPa to the top of the troposphere for MERRA-2, and between 925 and 600 hPa for NCEP2; the northern descending branch, which is also very strong, is visible and consistently represented by the three reanalysis products. Apart from REMO-NorESM1 (which makes visible a small part of the southern downward branch and shrinks the band of the upward component), other REMO experiments feature a similar cell pattern. However, these runs model stronger values of the ascending branch inside the region. Likewise, except for RegCM4-NorESM1, which behaves like its counterpart REMO-NorESM1, the rest of the RegCM4 simulations show a similar cell with reanalyses. However, some runs (e.g., RegCM4-ERA, RegCM4-HadGEM2, and RegCM4-NorESM1) produce a weaker cell intensity, whereas the other (RegCM4-MPI-MR) shows values within the range of reanalyses. In SON (Fig. 11b), reanalyses show that a part of the southern downward branch appears and part of the northern branch slightly weakens compared to what is observed in MAM. REMO-ERA features a stronger southern descending branch and similar ascending and northern downward branches with reanalyses. Other REMO-ESMs display a weaker and narrow rising component in midlayers (700–500 hPa). RegCM4-ERA and RegCM4-HadGEM2 highly underestimate the SON Hadley cell elsewhere. RegCM4-MPI-MR and RegCM4-NorESM1 model a stronger southern downward component, and a weaker and shrinking ascending branch.

The hypothesis of a better integrated Walker-type cell in RCMs relative to the Hadley-like circulation, made in section 5a, is confirmed. RCMs broadly outperform in representing $\psi_z$. Given the known link between the Hadley circulation and the convection over central Africa, the biased Hadley circulation may also introduce biases in simulated convection, because the convection is the ascending branch of the Hadley cell over central Africa (Fierro et al. 2009). Kamae et al. (2011) showed that over the tropics (10°S–15°N), the weakening of the Hadley circulation is the response of strong deep convection. Also, the climatological variability of the Hadley cell strongly correlates with the zonal mean annual total precipitation (Stachnik and Schumacher 2011). Therefore an anomalously modeled weak or strong Hadley cell might suggest an anomalously modeled strong or weak convection. This is assessed below.

## 6. The local convection

Precipitation over CEA mainly originates from convection (Washington et al. 2013; Cook and Vizy 2016). This section ends analyses by assessing the feedback of simulated local convection to modeled zonal and meridional atmospheric circulation. It should be noted that in these hydrostatic versions of REMO2015 and RegCM4-v7, convection is parameterized and not explicitly resolved. Therefore here we are analyzing the wind vertical velocity, which can be associated with convection. Some physical and thermodynamic drivers are also investigated to understand the reasons behind simulated convection characteristics. The analysis is also separated into the WCEA and ECEA, based on different behaviors of models of the atmospheric circulation over the two areas (Figs. 8, 10, and 11). There are no vertical velocity data available from RegCM4-v7. Therefore, analyses are done only with REMO2015 outputs. However, based on previous analyses and on the REMO2015 results of the convection, conclusions could be reached.

In WCEA (Fig. 12; see also Fig. S8) and in MAM (Fig. 12; see also Fig. S8a), vertical motion is weak in the lower layers

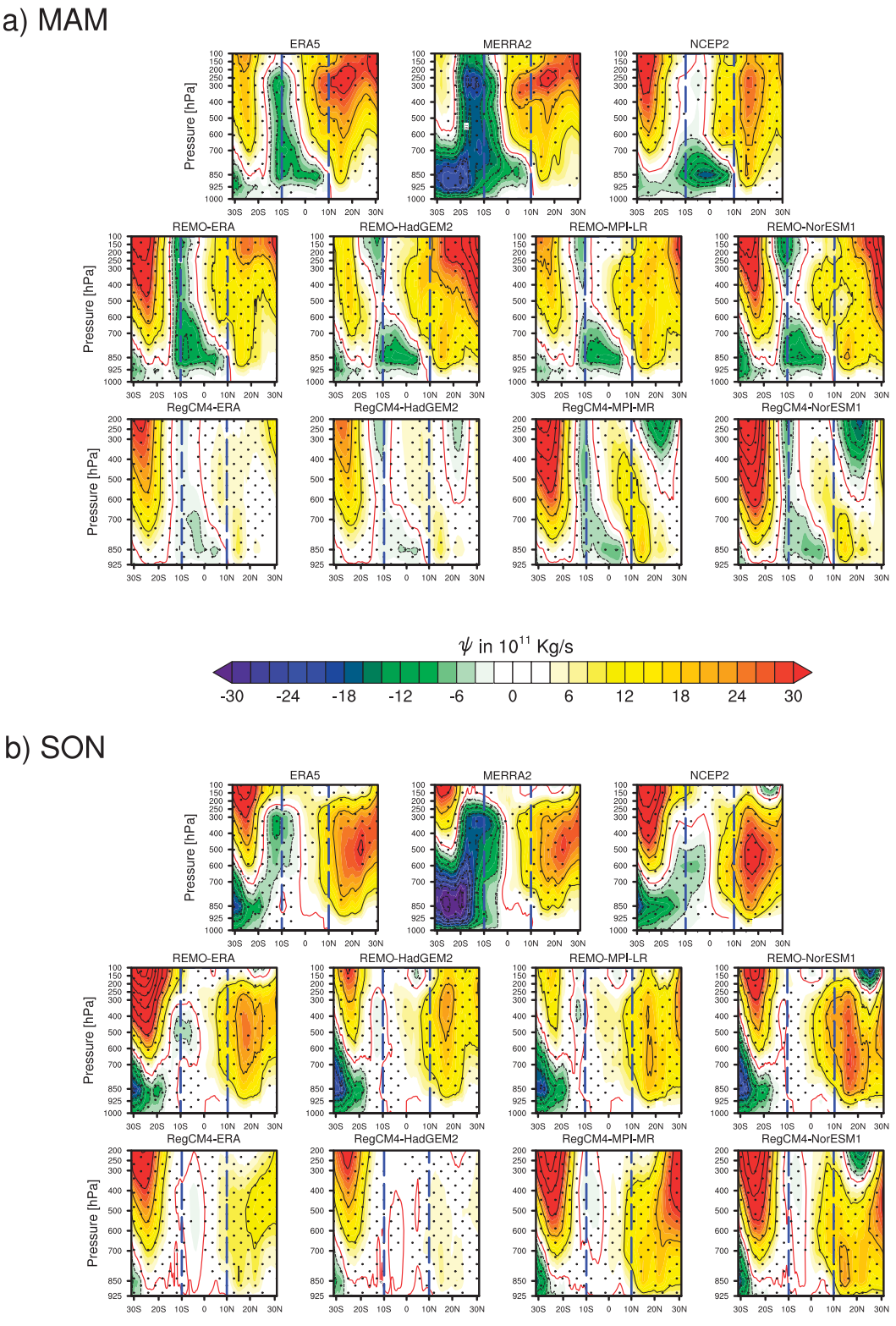


FIG. 10. Zonal average of the long-term seasonal mean (1980–2005) (a) MAM and (b) SON meridional mass-weighted streamfunction values ($\psi_M$; contours in $\times 10^{11}$ kg s$^{-1}$) over the WCEA (longitudes 10°–25°E). Data used are from reanalysis ERA5, MERRA-2, and NCEP2, and for the REMO2015 and RegCM4-v7 experiments. Positive values (solid contours) represent the counterclockwise circulation while negative values are the clockwise circulation.

(<700 hPa) and becomes strong in the upper layers (>700 hPa), provoking deep convection up to 200 hPa, consistently represented by the three reanalyses. MERRA-2, which features a higher rainfall rate, also features higher omega ($\omega$) values ($-0.23$ m s$^{-1}$). NCEP2, characterized by a weaker rainfall rate, also shows weaker $\omega$ values ($-0.007$ m s$^{-1}$). All REMO experiments, which overestimated precipitation over this area, also simulated strong values of $\omega$, within the range $-0.17$ m s$^{-1}$ (REMO-ERA) to $-0.23$ m s$^{-1}$ (REMO-HadGEM2). A rainier SON (Fig. 12b; see also Fig. S8b) than MAM, associated with intensification of the convection, presents in the three reanalyses (with values reaching $-0.20$ m s$^{-1}$ for ERA5, $-0.25$ m s$^{-1}$ for MERRA-2, and $-0.13$ m s$^{-1}$ for NCEP2). REMO runs generally behave in the same way as reanalyses but with the largest values of vertical motion included in the range $-0.17$ m s$^{-1}$ for REMO-ERA and $-0.31$ m s$^{-1}$ for REMO-MPI-LR.

In ECEA (Fig. 13; see also Fig. S8), the observed pattern of the convection is somewhat identical to what is observed in WCEA in the two seasons (Figs. 13a,b and S8a,b), but with a slightly more intense intensity (values within the from range $-0.007$ m s$^{-1}$ for NCEP2 to $-0.25$ m s$^{-1}$ for MERRA-2 in MAM; between $-0.13$ m s$^{-1}$ for NCEP2 and 0.27 m s$^{-1}$ for MERRA-2 in SON), corresponding to high precipitation. All REMO simulations fail in capturing the ECEA convection. They present stronger subsidences in lower layers (1000–850 hPa) over the southern latitudes, and stronger but shallow ascents in the midtroposphere, which are less precipitating. These shallow ascents intensify in SON while lower-layer subsidence decreases, justifying slight increases in rainfall amount.

Thus, the model patterns of the convection both in WCEA and ECEA match well with their dipole rainfall biases. However, it should be noted that although an increase in vertical motion is a strong indication of tropical convection, enhanced convection does not necessarily mean a strengthened rainfall over the Congo basin (WCEA; Hamada et al. 2015; Raghavendra et al. 2018; Alber et al. 2021). These studies showed increased thunderstorms over the WCEA, but contrastingly with the observed drying trend. To understand the reasons for RCMs' convection biases, we first explored biases in the simulated physical forcing which is the topography as shown in Fig. 14. One of the advantages of downscaling is the better representation of the orography. To get an insight into the fitness of the downscaling, surface altitudes are computed from the annual mean surface pressure prognostic variable, using the barometric levelling equation, instead of directly using outputs of models of orography static variables. It emerges that the downscaling affords a substantial added value, as all RCM runs are capable to represent highlands of the WCEA (~15°E) and ECEA (the Rift Valley system; 30°–40°E) despite a slight underestimation of mountaintops relative to the GTOPO30 digital elevation model. The coarse-resolution NCEP2 is not able to capture mountaintops. A recent work by Munday et al. (2021) also showed that comparable coarse-resolution CMIP5 ESMs fail in capturing the majority of highlands of eastern and southern Africa with adverse effects on the circulation. Therefore, the topography would not play an important role in modeled convection biases, especially in ECEA where vertical motion is mainly topographically constrained.

To this, we turned our attention to the thermodynamic conditions associated with the thermal state of atmospheric stability or instability (shallow or deep convection). The moist static energy (MSE) is a useful metric for the purpose and is defined as

$$\mathrm{MSE} = C_p T + gz + Lq \tag{1}$$

with the first two terms on the right-hand side representing the dry static energy (DSE) input; $C_pT$ is the sensible heat, $gz$ is the potential energy and $Lq$ is the latent static energy (LSE); $C_p$ is the specific heat at constant pressure, $T$ is the air temperature, $g$ is the gravitational constant, $z$ is the geopotential height, $L$ is the latent heat of condensation, and $q$ is the specific humidity. Figures 15 and 16 exhibit results respectively over WCEA, area of wet biases, and over ECEA, area of dry biases. Note that for all datasets, the equivalent potential temperature $\theta_e$ (Fig. S9 and Fig. S10) features a very similar vertical structure to that of MSE.

REMO products display high values of MSE over the WCEA and in the two seasons (Fig. 15), with values included in the range of reanalyses (the two datasets featuring values within the range $337.2 \leq \mathrm{MSE} \leq 342.7$ kJ kg$^{-1}$ in MAM, and $338.5 \leq \mathrm{MSE} \leq 341.6$ kJ kg$^{-1}$ in SON). RegCM4 simulations exhibit weaker MSE quantities, with values ranging from 333.7 kJ kg$^{-1}$ (RegCM4-MPI-MR) to 337.8 kJ kg$^{-1}$ (RegCM4-ERA) in MAM, 334.5 kJ kg$^{-1}$ (RegCM4-MPI-MR) to 336.4 kJ kg$^{-1}$ (RegCM4-ERA) in SON, matching their weaker convection amounts and patterns compared to REMO and reanalyses. The important role of thermodynamic biases in contributing to convection biases is highlighted. For instance, in MAM, the REMO/RegCM4-MPI-LR/MR runs that feature the weakest rainfall rate also show the narrowest convection band as indicated by the 330-K $\theta_e$ contour. Likewise, models generally better capture the convection band than the MSE and $\theta_e$, which stands for the lesser important role of the convection band biases. Over the ECEA and in

←

The solid red line is the $\psi_M = 0$ value. Contour intervals are $-4 \times 10^{11}$ kg s$^{-1}$ for negative values and $10 \times 10^{11}$ kg s$^{-1}$ for positive values. The stippling appears where the difference between the dataset under consideration and the ensemble mean of the three reanalysis products is statistically significant at the 95% confidence level by means of the Student's $t$ test. The blue bars delimit the latitudinal band of the WCEA.

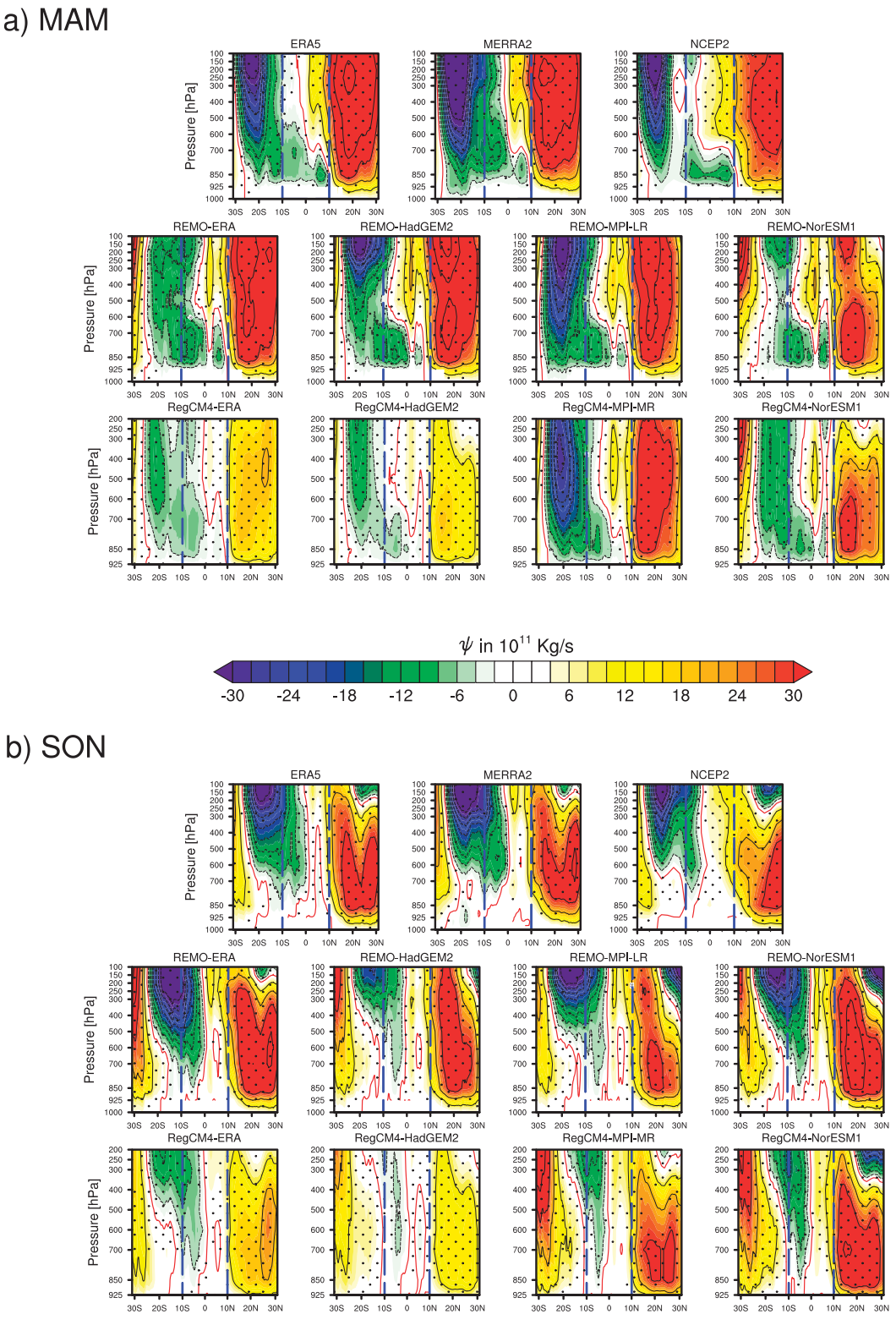


FIG. 11. As in Fig. 10, but for the ECEA (longitudes 25°–35°E).

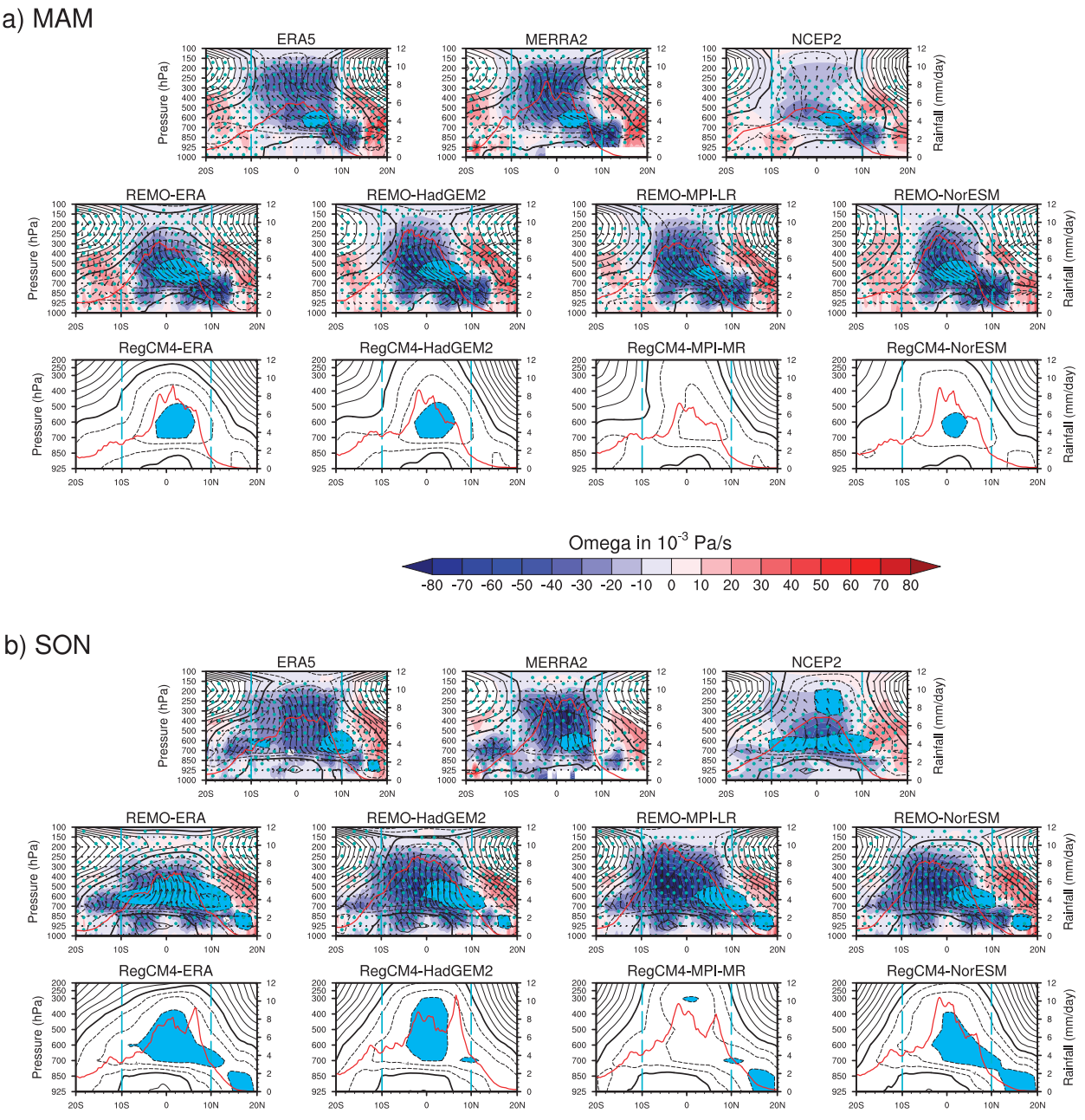


FIG. 12. Height–latitude cross section averaged over WCEA (longitude band 10°–25°E) of the vertical velocity ($\omega$; Pa s$^{-1}$; shaded), zonal wind ($u$; m s$^{-1}$; overlaid light-blue shaded areas), the vertical motion of meridional wind and omega (vectors), and the monthly precipitation (mm day$^{-1}$; red lines) in (a) MAM and (b) SON seasons. Data used are from ERA5, MERRA-2 and NCEP2 reanalysis data, and from the REMO2015 and RegCM4-v7 experiments over the period 1980–2005. The vertical velocity data are not available for RegCM4-v7 experiments. The stippling indicates the grid points where the difference between the dataset under consideration and the ensemble mean of the three reanalysis products is statistically significant at the 95% confidence level using the Student's $t$ test. The cyan bars delimit the WCEA latitudinal band.

the two seasons (Fig. 16), all experiments model weaker MSE relative to all reanalyses, corresponding to the weaker convection rate recorded. Reanalyses feature MSE values within the ranges of 340 ≤ MSE ≤ 342.4 kJ kg$^{-1}$ in MAM and 338.6 ≤ MSE ≤ 341 kJ kg$^{-1}$ in SON. REMO runs do so, ranging from 336.1 kJ kg$^{-1}$ (REMO-MPI-LR) to 340 kJ kg$^{-1}$ (REMO-ERA), and RegCM4 experiments have values between 333.3 kJ kg$^{-1}$ (RegCM4-MPI-MR) and 337 kJ kg$^{-1}$ (RegCM4-ERA) in MAM, and between 336.7 kJ kg$^{-1}$ (REMO-MPI-LR) and 338.8 kJ kg$^{-1}$ (REMO-ERA), and

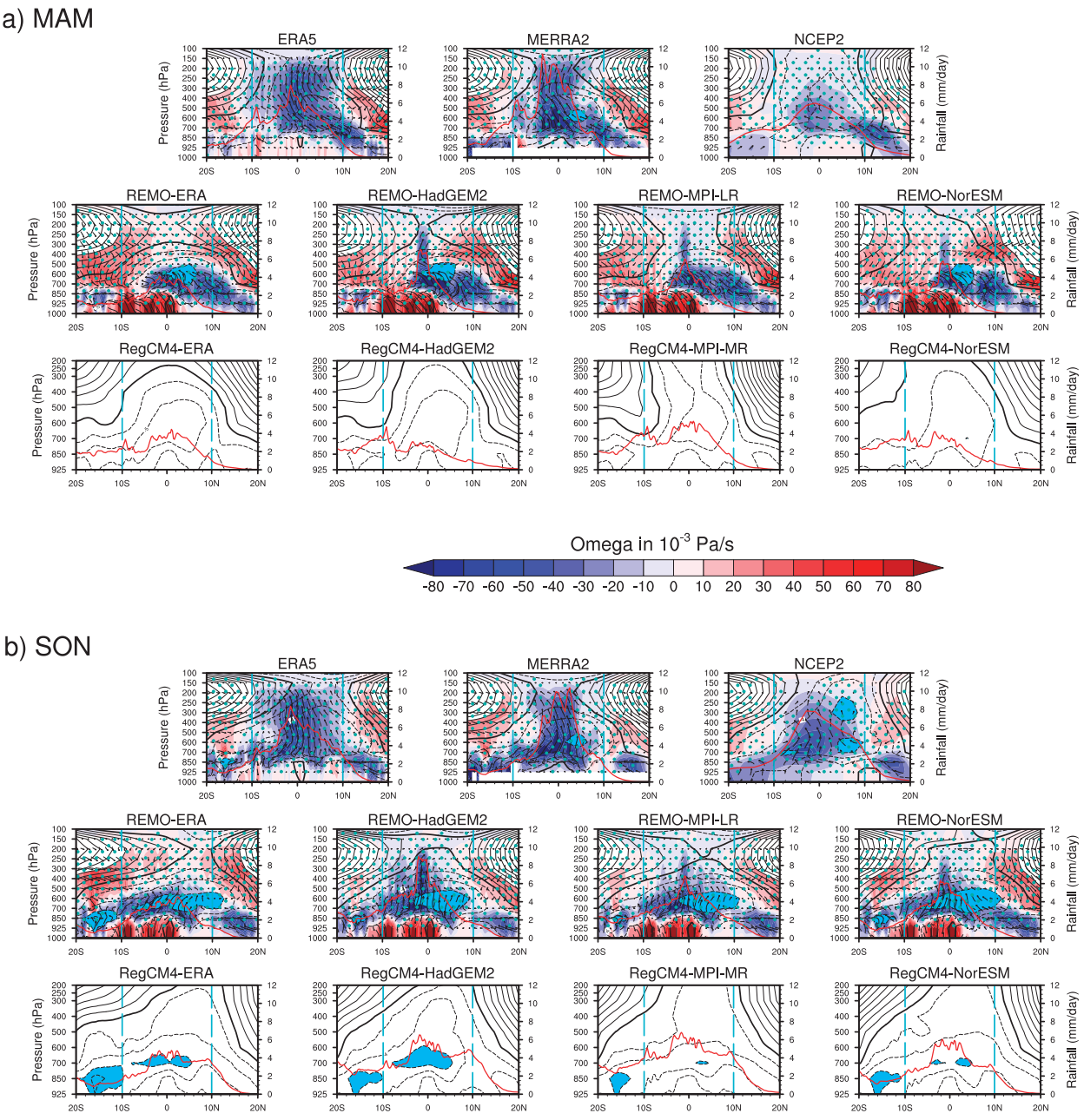


FIG. 13. As in Fig. 12, but for the ECEA (longitude band 25°–35°E).

RegCM4 experiments between 334 kJ $kg^{-1}$ (RegCM4-MPI-MR) and 335.6 kJ $kg^{-1}$ (RegCM4-ERA) in SON. Apart from REMO-ERA, other runs show a more shrunken convection band than in reanalyses.

During the two seasons and both west and east CEA, all datasets feature consistent DSE (not shown), thus suggesting its irrelevance in the model biases. However, models simulate strong specific humidity in WCEA, and weak in ECEA (not shown), which would lead, correspondingly, to a modeled higher and lower LSE over the respective areas. This means that the LSE component has played a crucial role in determining models of atmospheric instability or stability, and therefore models' wetness or dryness.

## 7. Conclusions and discussion

This study explored misrepresented mechanisms associated with CORDEX-CORE (REMO2015 and RegCM4-v7) rainfall biases over CEA. The motivation is based on the

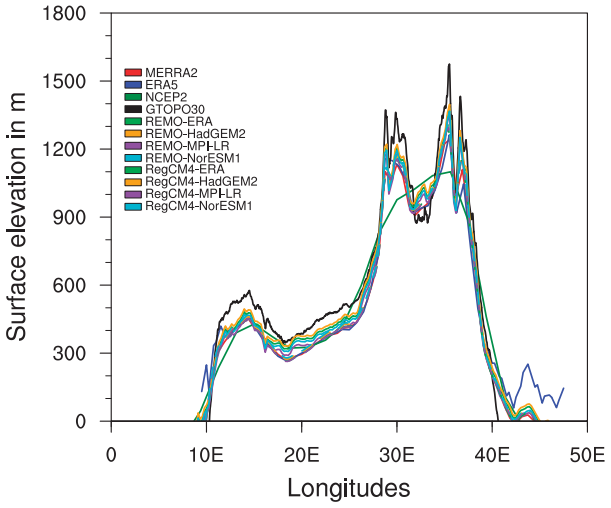


FIG. 14. Longitudinal cross section of surface elevation (in m) across the CEA, averaged over latitudes 5°S–5°N, for reanalysis data MERRA-2, ERA5, and NCEP2 and for REMO2015 (solid lines) and for the RegCM4-v7 (dashed lines) experiments. The NASA GTOPO30 (black line) is used as a point of reference. Surface altitudes are computed from the surface pressure data, using the barometric levelling equation.

need to assess the credibility of these RCMs in modeling the CEA's climate system and stimulate discussions about challenges and opportunities of their application for climate change evaluations. Analysis was focused on some of its better-known climate system drivers, comprising land–sea interactions through local SSTs, MSLPs, and changes in the surface pressure, and regional atmospheric circulations such as low-level westerlies, the Congo basin cell, the Hadley-like circulation, midlevel easterly jets, and convection. A dipole-like rainfall bias is found at rainfall peaks (MAM and SON) in all experiments, consisting of positive biases in WCEA and negative biases in ECEA. Throughout the analyses, the two RCMs featured similar characteristics of analyzed processes, although some of them have not been diagnosed (e.g., convection) or have only been partially diagnosed (e.g., the 1000-hPa level of the Congo basin cell) for the RegCM4 RCM, owing to the lack of necessary data. Potential mechanisms to be drivers of the western and eastern CEA precipitation biases in the two RCMs are as follows (see Fig. 17 for the schematic illustration):

1) RCM experiments generally simulate weaker MSLPs, including the South Atlantic high pressure system. As a first consequence, less moisture is transported from the Atlantic Ocean toward coastal regions of the basin.
2) The second impact of simulated weaker MSLPs is the modeling of a land–ocean $\nabla P$ not strong enough for REMO runs or underestimated for RegCM4 ones, necessary for importing important moisture amounts from the western border toward the eastern.
3) Given that $\nabla P$ is not strong enough (in REMO) or weaker (in RegCM) in MAM, the modeled Congo basin cell intensity is also weaker (corresponding to slower LLWs) and is in a farther west position at this time of the year. Although this position is favorable to the advection of large amounts of moisture (Longandjo and Rouault 2020), the cell intensity is weak, resulting in low penetration of moisture into the region. Otherwise, the strength of the cell is low to move the amount of moisture required eastward, therefore provoking an uneven distribution of moisture across the region. Beside this, are advected southeasterlies that recurve into southerlies while crossing the southern border and overfeed the western sector. Consequently, moisture availability is stronger over the WCEA than ECEA. Models of $\nabla P$ slightly intensify in SON, which accentuates inward moisture, thus increasing the moisture availability into the domain, both in west and east.
4) The local evaporation might have also contributed to the rainfall dry biases over the ECEA through the recycling. As shown in Fig. S7, all RCM runs produce stronger evaporation dry biases over the eastern than western CEA.
5) The atmospheric instability is high in all experiments in WCEA but is strongly underestimated in ECEA. In fact, mass convergence is slow due to a weak Congo basin cell strength and thereby weak LLWs. As a result, the moist air accumulates much more to the west of the region, increasing the atmospheric instability through the increased moist static energy (MSE), and which leads to convection. A weak Congo basin cell may also have contributed to little moisture transported toward the eastern border where it arrives at a slower pace. This leads to a weaker MSE. Therefore, the intensity of uplifted moisture is low to destabilize the atmospheric stability in bottom layers, which is needed to initialize upward motions and thus the convection.
6) Hadley-like circulation biases are associated with convective biases. The intense convection in the western part of the CEA weakens the ascending branch of the Hadley circulation over the same area, while the reduced convection over the eastern part, in contrast, strengthens the cell over the corresponding region (Kamae et al. 2011).
7) The role of AEJs is not marginal, especially in SON. Whether AEJ-N has been relatively correctly reproduced by most RCM runs in MAM, the positioning and intensity of both AEJ-N and AEJ-S cores are misrepresented in SON. Here, RCM experiments simulating a single and stronger AEJ-N also simulate stronger northern and eastern rainfall dry biases. In fact, a stronger jet induces intense moisture divergence across the region (Dyer et al. 2017), which in turn would reduce MCSs due to reduced moisture availability, thereby suppressing the convection (Jackson et al. 2009). Other runs that produce a single and relatively normal AEJ-N or equatorward jet, and thus broadly weaker midlevel jets, model a higher rainfall amount, related to the increased midlevel moisture availability that feeds the convection (Dezfuli and Nicholson 2013).

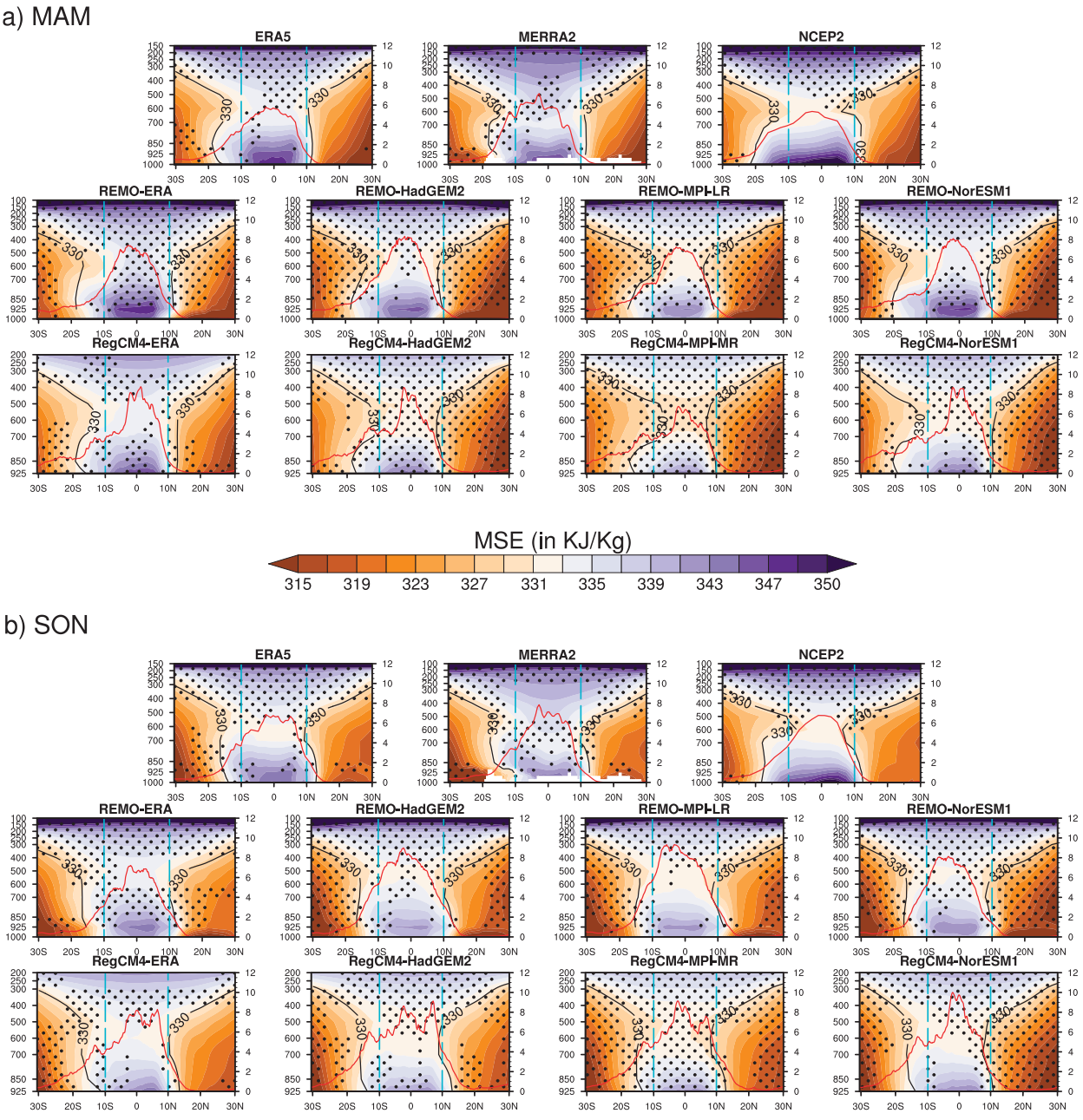


FIG. 15. Latitude–height cross sections of the moist static energy (MSE; kJ $kg^{-1}$) in (a) MAM and (b) SON seasons over the WCEA (averaged over longitudes 10°–25°E). Data used are from reanalysis data (ERA5, MERRA-2, and NCEP2) and from the REMO2015 and RegCM4-v7 experiments over the period 1980–2005. The 330-K contour of the equivalent potential temperature ($\theta_e$; black line) highlights the convection band. The red lines are latitudinal migration of the rainband (mm $day^{-1}$). The stippling occurs where the difference between the dataset under consideration and the ensemble mean of the three reanalysis products is statistically significant at the 95% confidence level by means of the Student's *t* test. The cyan bars delimit the CEA latitudinal band.

The complexity of modeling the Congo basin climate system lies beforehand in the multitude of physical processes that interact at various scales (local, regional, and large scales). Although they are accounted for during the downscaling process, some large-scale phenomena (e.g., ENSO, the Indian Ocean dipole, the MJO) unfortunately cannot be diagnosed owing to the limited geographical area. They would have played a determining role in rainfall biases at a local or regional scale. In addition, this region features one of the most understudied climate systems, and whose physical drivers and mechanisms are progressively documented. Based on this observation, we cannot claim to have highlighted all the

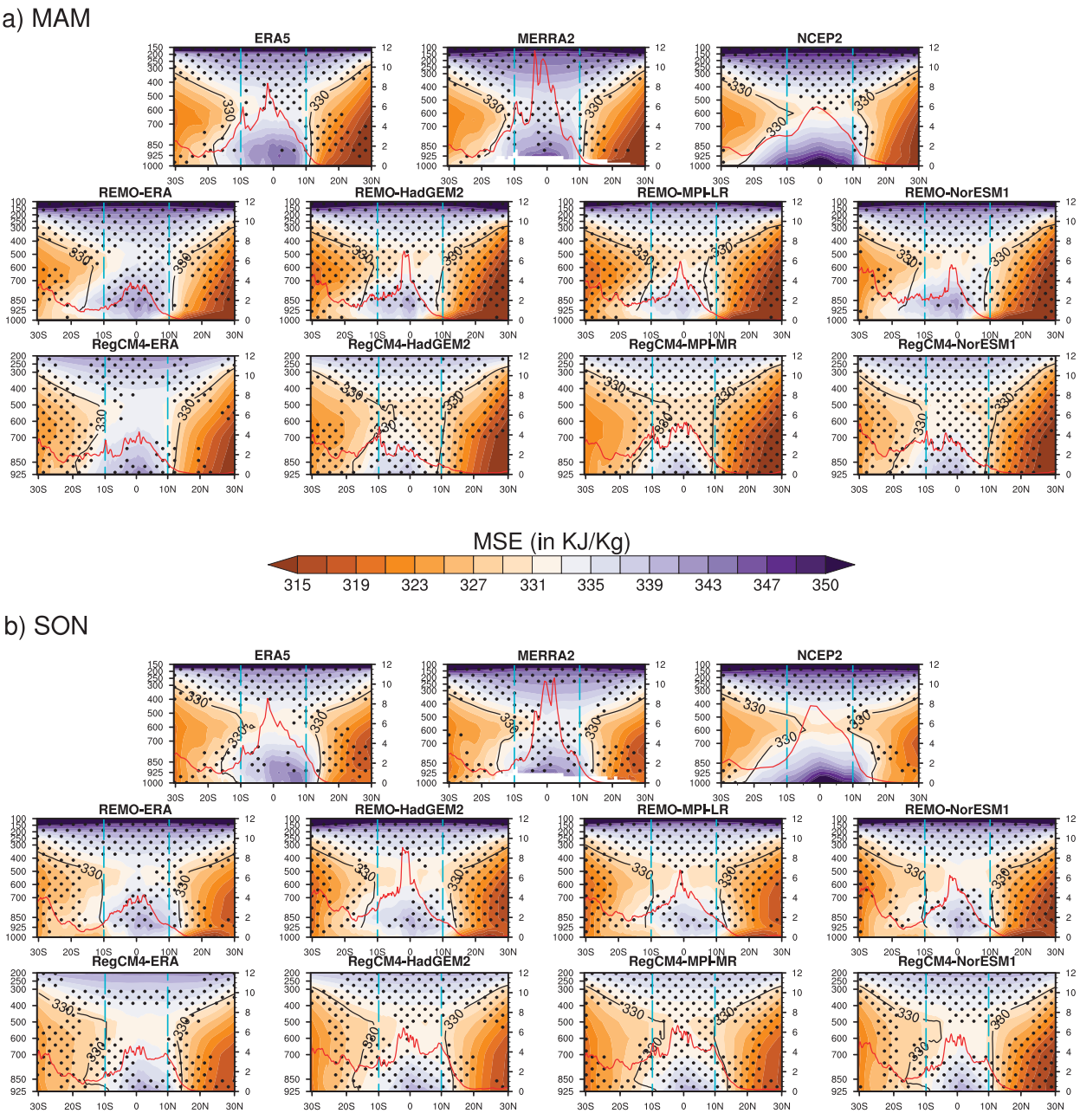


FIG. 16. As in Fig. 15, but for the ECEA (averaged over longitudes 25°–35°E).

misrepresented mechanisms associated with simulated rainfall biases over CEA. Nevertheless, RCMs used in this study realistically represent the basic structures of already known mechanisms modulating its climate system. Since climate model outputs are imperfect, the process-based assessment approach is very useful for selecting models that can project plausible future climate change signals. James et al. (2018) argued that models that produce uncoupled diagnostic variables with associated dynamics cannot be considered reliable for simulating future climate; rather, the plausibility of a modeled climate change signal is conditioned by the ability of the model to reproduce the corresponding change signal in the observed related mechanism. These conclusions are relevant in the use of above RCM projections of future rainfall in the region under anthropogenic climate change. Another important limitation of this study lies in the RCMs' configuration. For instance, the convection is parameterized, and RCMs are not coupled with an ocean model, as they do not physically modify SSTs prescribed by ESMs. Further studies could be conducted with convection-permitting RCMs and regionally coupled atmosphere–ocean RCMs. These could prompt the next steps of our study.

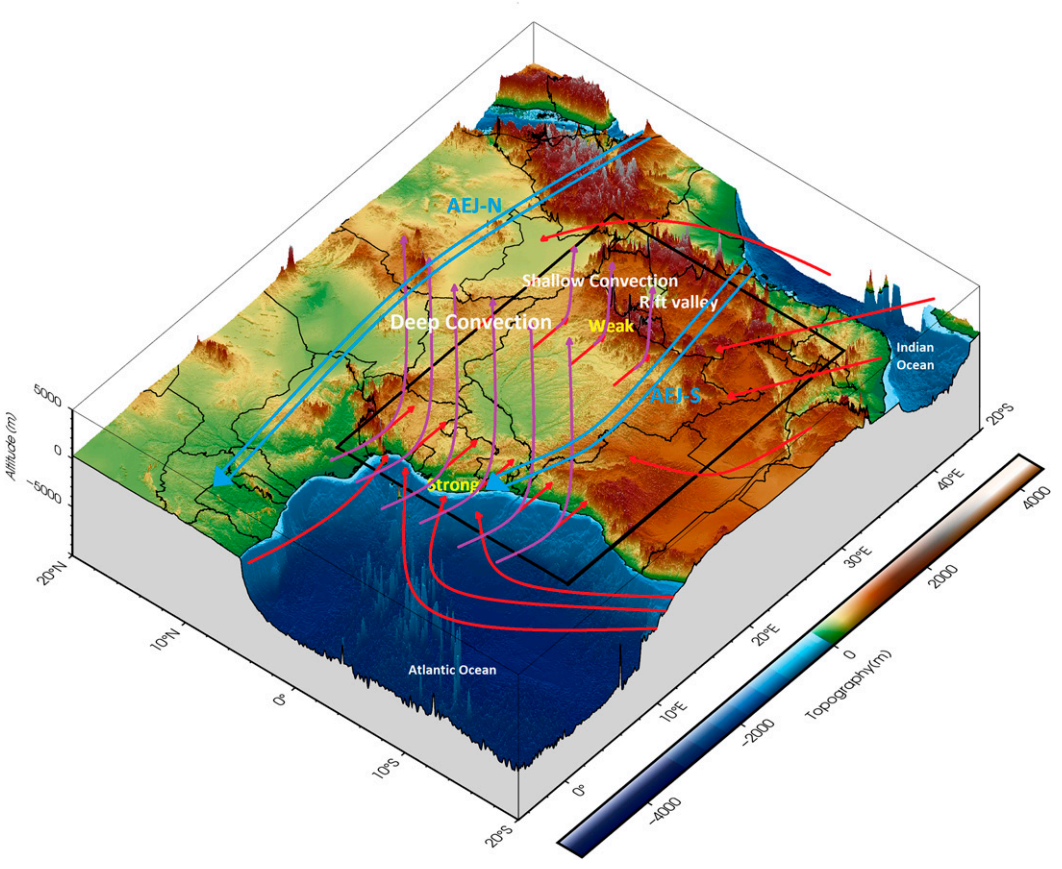


FIG. 17. Three-dimensional schematic of topography (m; shaded, using data from the NASA GTOPO30) and wind flow over central equatorial Africa. Red arrows indicate low-level circulation. Purple arrows show the ascent motion. The two large blue arrows highlight the area of interaction of the two components of the African easterly jet (AEJ), the northern branch (AEJ-N), and the southern branch (AEJ-S).

*Acknowledgments.* This research is supported by DAAD within the framework of the ClimapAfrica programme with funds of the Federal Ministry of Education and Research (funding ID 57556650 and reference 91795180). The publisher is fully responsible for the content. We also thank the Climate Service Center (GERICS), and the Earth System Physics (ESP) section of the International Centre for Theoretical Physics (ICTP) for performing respectively REMO2015 and RegCM4-v7 simulations. These data are made available through the Earth System Grid Federation (ESGF) website (https://esgf-data.dkrz.de/search/cordex-dkrz/). Thank you to all the reanalysis, satellite, and observational data providers used in this study. The authors thank the three anonymous reviewers and the editor whose comments helped improve and clarify this manuscript. The authors declare that they have no conflict of interest.

*Data availability statement.* REMO2015 and RegCM4-v7 output data are available through the Earth System Grid Federation (ESGF) website (https://esgf-data.dkrz.de/search/cordex-dkrz/). The ERA-Interim reanalysis is available from the European Centre for Medium-Range Weather Forecast (ECMWF) and can be downloaded through the link https://apps.ecmwf.int/datasets/data/interim-full-daily/levtype=sfc/. The ERA5 reanalysis is produced within the Copernicus Climate Change Service (C3S) by the ECMWF and is accessible via the link https://cds.climate.copernicus.eu/cdsapp#!/dataset/reanalysis-era5-pressure-levels-monthly-means?tab1/4form. The MERRA-2 reanalysis, developed by the NASA, is available online (https://disc.gsfc.nasa.gov/datasets?keywords1/4%22MERRA-2%22&page1/41&source1/4Models%2FAnalyses%20MERRA-2). The NCEP2 dataset is provided by the NOAA/OAR/ESRL PSD and is available through the website https://psl.noaa.gov/data/gridded/data.ncep.reanalysis2.html. The GPCC observational data set is available at https://opendata.dwd.de/climate_environment/GPCC/html/fulldata-monthly_v2020_doi_download.html. The GPCP-v2.3 combined precipitation dataset is available at https://www.esrl.noaa.gov/psd/data/gridded/data.gpcp.html; the CRU-v4.04 dataset is available at https://data.ceda.ac.uk/badc/cru/data/cru_ts/cru_ts_4.04/data/pre (UEA, 2019). The UDel-4.01 dataset is available at http://climate.geog.udel.edu/climate/html_pages/download.html. The CHIRPS2 data are available at https://data.chc.ucsb.edu/products/CHIRPS-2.0/global_daily/netcdf/. The corresponding author is available for providing NIC131 data upon request. ARC2 data are available at http://iridl.ldeo.columbia.edu/

SOURCES/.NOAA/.NCEP/.CPC/.FEWS/.Africa/.DAILY/.ARC2/.daily/. The UGDP is available at https://psl.noaa.gov/data/gridded/data.cpc.globalprecip.html. The HadISST SST data are available at https://www.metoffice.gov.uk/hadobs/hadisst/data/download.html. Finally, the ERSST-v5 SST data are available at https://psl.noaa.gov/data/gridded/data.noaa.ersst.v5.html.

## APPENDIX A

### The Regional Moisture Convergence/Divergence Calculations

The vertically integrated moisture transport is obtained using the following equation:

$$QV = \frac{1}{g}\int_{\mathrm{sp}}^{P_{\mathrm{top}}} qV dp, \tag{A1}$$

where $QV$ can be rewritten as

$$QV = (Q_u, Q_v), \tag{A2}$$

where $Q_u$ (kg m$^{-1}$ s$^{-1}$) is the zonal moisture transport and $Q_v$ (kg m$^{-1}$ s$^{-1}$) is the meridional moisture transport; also, $V$ (m s$^{-1}$) is the total wind field, decomposed into its zonal $u$ and meridional $v$ components, $g$ is the gravitational acceleration (m s$^{-2}$), $q$ is the specific humidity (g kg$^{-1}$), sp is the surface pressure, and $P_{\mathrm{top}}$ is the pressure of the top level (Pa). To highlight sources of moisture surplus or deficit, the transient regional moisture convergence or divergence across each CEA border and at each pressure level was estimated. In a given region, the total moisture convergence/divergence is the sum of inflows/outflows across frontiers, which can be split into the zonal (west–east; $Q_\lambda$) and the meridional (south–-north; $Q_\phi$) directions as follows:

$$Q_\lambda = \frac{1}{g}\int qud\lambda \tag{A3}$$

and

$$Q_\phi = \frac{1}{g}\int qvd\phi, \tag{A4}$$

where $\lambda$ are longitudes and $\phi$ latitudes. The region can be considered as a rectangle of length $X$ and width $Y$, with $X$ and $Y$ being a set of segments $dl$ through which, the atmospheric moisture is inwards and outwards. Thereby, transient moisture across west ($Q_{\lambda_{\mathrm{west}}}$), east ($Q_{\lambda_{\mathrm{east}}}$), south ($Q_{\phi_{\mathrm{south}}}$), and north ($Q_{\phi_{\mathrm{north}}}$) can be expressed as follows:

$$Q_{\lambda_{\mathrm{west}}} = \int_{l_{\mathrm{west}}} Q_\lambda dl \text{ and } Q_{\lambda_{\mathrm{east}}} = \int_{l_{\mathrm{east}}} Q_\lambda dl, \tag{A5}$$

$$Q_{\phi_{\mathrm{south}}} = \int_{l_{\mathrm{south}}} Q_\phi dl \text{ and } Q_{\phi_{\mathrm{north}}} = \int_{l_{\mathrm{north}}} Q_\phi dl, \tag{A6}$$

where

$$dl = \theta \times \frac{\pi}{180} \times R, \tag{A7}$$

with $\theta$ being the dataset's horizontal resolution in the zonal or meridional direction, and $R$ (m) Earth's radius, and

$$l_{\mathrm{west}} = 10°\mathrm{E},\ l_{\mathrm{east}} = 35°\mathrm{E},\ l_{\mathrm{south}} = 10°\mathrm{S}, \text{ and } l_{\mathrm{north}} = 10°\mathrm{N}.$$

The net zonal ($Q_z$), meridional ($Q_m$), and total ($Q_T$) moisture are calculated as

$$Q_z = Q_{\lambda_{\mathrm{west}}} - Q_{\lambda_{\mathrm{east}}} \text{ and } Q_m = Q_{\phi_{\mathrm{south}}} - Q_{\phi_{\mathrm{north}}}, \tag{A8}$$

$$Q_T = Q_z + Q_m. \tag{A9}$$

## APPENDIX B

### Estimating the Congo Low-Level Cell and the Hadley-Like Circulation

Because of the crucial importance of regional circulations for modulating the CEA precipitation system, we have diagnosed the state of zonal low-level and meridional cells associated with their drivers (Kamae et al. 2011; Longandjo and Rouault 2020) in RCM experiments. Note that these cell systems summarize the majority of processes depicted as mediators of low-level circulations (e.g., Dezfuli and Nicholson 2013; Nicholson and Dezfuli 2013; Pokam et al. 2014; Dezfuli et al. 2015; Cook and Vizy 2016). For this purpose, the water vapor mass transported within the mean zonal ($\psi_Z$) and mean meridional ($\psi_M$) circulations are estimated by the means of the mass-weighted streamfunctions ($\psi$; e.g., Stachnik and Schumacher 2011) using respectively the following equations:

$$\psi_Z = \frac{2\pi R}{g}\int_{\mathrm{sp}}^{P} [u] dp, \tag{B1}$$

and

$$\psi_M = \frac{2\pi R\cos\phi}{g}\int_{\mathrm{sp}}^{P} [v] dp, \tag{B2}$$

where $\pi$ is a circular constant, sp the surface pressure, and $P \in$ [1000–100 hPa], while the square brackets indicate a zonal or meridional average. Using these two indices enables one to get an insight into the way the models reproduce regional-scale Walker- and Hadley-like circulations (Oort and Yienger 1996; Stachnik and Schumacher 2011; Kamae et al. 2011) over the region, both in terms of strength and width.

## REFERENCES


Alber, K., A. Raghavendra, L. Zhou, Y. Jiang, H. S. Sussman, and S. L. Solimine, 2021: Analyzing intensifying thunderstorms over the Congo Basin using the Gálvez-Davison index from 1983–2018. *Climate Dyn.*, **56**, 949–967, https://doi.org/10.1007/s00382-020-05513-x.

Baccini, A., and Coauthors, 2012: Estimated carbon dioxide emissions from tropical deforestation improved by carbon-density maps. *Nat. Climate Change*, **2**, 182–185, https://doi.org/10.1038/nclimate1354.

Balas, N., S. E. Nicholson, and D. Klotter, 2007: The relationship of rainfall variability in West Central Africa to sea-surface temperature fluctuations. *Int. J. Climatol.*, **27**, 1335–1349, https://doi.org/10.1002/joc.1456.

Bell, J. P., A. M. Tompkins, C. Bouka-Biona, and I. S. Sanda, 2015: A process-based investigation into the impact of the Congo basin deforestation on surface climate. *J. Geophys. Res.*, **120**, 5721–5739, https://doi.org/10.1002/2014JD022586.

Bentsen, M., and Coauthors, 2013: The Norwegian Earth System Model, NorESM1-M—Part 1: Description and basic evaluation of the physical climate. *Geosci. Model Dev.*, **6**, 687–720, https://doi.org/10.5194/gmd-6-687-2013.

Chen, T., 2004: Maintenance of the midtropospheric North African summer circulation: Saharan high and African easterly jet. *J. Climate*, **18**, 2943–2962, https://doi.org/10.1175/JCLI3446.1.

Collins, W. J., and Coauthors, 2011: Development and evaluation of an Earth system model—HadGEM2. *Geosci. Model Dev.*, **4**, 1051–1075, https://doi.org/10.5194/gmd-4-1051-2011.

Cook, K. H., and E. K. Vizy, 2006: Coupled model simulations of the West African monsoon system: Twentieth- and twenty-first-century simulations. *J. Climate*, **19**, 3681–3703, https://doi.org/10.1175/JCLI3814.1.

——, and ——, 2016: The Congo Basin Walker circulation: Dynamics and connections to precipitation. *Climate Dyn.*, **47**, 697–717, https://doi.org/10.1007/s00382-015-2864-y.

——, Y. Liu, and E. K. Vizy, 2020: Congo Basin drying associated with poleward shifts of the African thermal lows. *Climate Dyn.*, **54**, 863–883, https://doi.org/10.1007/s00382-019-05033-3.

Creese, A., and R. Washington, 2016: Using qflux to constrain modeled Congo Basin rainfall in the CMIP5 ensemble. *J. Geophys. Res. Atmos.*, **121**, https://doi.org/10.1002/2016JD025596.

——, and ——, 2018: A process-based assessment of CMIP5 rainfall in the Congo Basin: The September–November rainy season. *J. Climate*, **31**, 7417–7439, https://doi.org/10.1175/JCLI-D-17-0818.1.

Dargie, G. C., S. L. Lewis, I. T. Lawson, E. T. Mitchard, S. E. Page, Y. E. Bocko, and S. A. Ifo, 2017: Age, extent and carbon storage of the central Congo Basin peatland complex. *Nature*, **542**, 86–90, https://doi.org/10.1002/qj.828.

Dee, D. P., and Coauthors, 2011: The ERA-Interim reanalysis: Configuration and performance of the data assimilation system. *Quart. J. Roy. Meteor. Soc.*, **137**, 553–597, https://doi.org/10.1002/qj.828.

Dezfuli, A. K., and S. E. Nicholson, 2013: The relationship of rainfall variability in western equatorial Africa to the tropical oceans and atmospheric circulation. Part II: The boreal autumn. *J. Climate*, **26**, 66–84, https://doi.org/10.1175/JCLI-D-11-00686.1.

——, B. F. Zaitchik, and A. Gnanadesikan, 2015: Regional atmospheric circulation and rainfall variability in south equatorial Africa. *J. Climate*, **28**, 809–818, https://doi.org/10.1175/JCLI-D-14-00333.1.

Dickinson, R., R. Errico, F. Giorgi, and G. Bates, 1989: A regional climate model for the western United States. *Climatic Change*, **15**, 383–422, https://doi.org/10.1007/BF00240465.

Dosio, A., and H. Panitz, 2016: Climate change projections for CORDEX-Africa with COSMO-CLM regional climate model and differences with the driving global climate models. *Climate Dyn.*, **46**, 1599–1625, https://doi.org/10.1007/s00382-015-2664-4.

——, and Coauthors, 2021a: Projected future daily characteristics of African precipitation based on global (CMIP5, CMIP6) and regional (CORDEX, CORDEX-CORE) climate models. *Climate Dyn.*, **57**, 3135–3158, https://doi.org/10.1007/s00382-021-05859-w.

——, I. Pinto, C. Lennard, M. B. Sylla, C. Jack, and G. Nikulin, 2021b: What can we know about recent past precipitation over Africa? Daily characteristics of African precipitation from a large ensemble of observational products for model evaluation. *Earth Space Sci.*, **8**, e2020EA001466, https://doi.org/10.1029/2020EA001466.

Dyer, E. L., D. B. Jones, J. Nusbaumer, H. Li, O. Collins, G. Vettoretti, and D. Noone, 2017: Congo Basin precipitation: Assessing seasonality, regional interactions, and sources of moisture. *J. Geophys. Res. Atmos.*, **122**, 6882–6898, https://doi.org/10.1002/2016JD026240.

Fierro, A. O., J. Simpson, M. A. Lemone, J. M. Straka, and B. F. Smull, 2009: On how hot towers fuel the Hadley cell: An observational and modeling study of line-organized convection in the equatorial trough from TOGA COARE. *J. Atmos. Sci.*, **66**, 2730–2746, https://doi.org/10.1175/2009JAS3017.1.

Fotso-Nguemo, T. C., D. A. Vondou, W. M. Pokam, Z. Y. Djomou, I. Diallo, A. Haensler, and C. Tchawoua, 2017: On the added value of the regional climate model REMO in the assessment of climate change signal over Central Africa. *Climate Dyn.*, **49**, 3813–3838, https://doi.org/10.1007/s00382-017-3547-7.

——, and Coauthors, 2021: Potential impact of 1.5, 2 and 3°C global warming levels on heat and discomfort indices changes over Central Africa. *Sci. Total Environ.*, **804**, 150099, https://doi.org/10.1016/j.scitotenv.2021.150099.

Funk, C., and Coauthors, 2015: The Climate Hazards Infrared Precipitation with Stations—A new environmental record for monitoring extremes. *Sci. Data*, **2**, 150066, https://doi.org/10.1038/sdata.2015.66.

Garcin, Y., and Coauthors, 2018: Early anthropogenic impact on Western Central African rainforests 2,600 y ago. *Proc. Natl. Acad. Sci. USA*, **115**, 3261–3266, https://doi.org/10.1073/pnas.1715336115.

Giorgi, F., 1989: Two-dimensional simulations of possible mesoscale effects of nuclear war fires: 1. Model description. *J. Geophys. Res.*, **94**, 1127, https://doi.org/10.1029/JD094iD01p01127.

——, and W. J. Gutowski, 2015: Regional dynamical downscaling and the CORDEX initiative. *Annu. Rev. Environ. Resour.*, **40**, 467–490, https://doi.org/10.1146/annurev-environ-102014-021217.

——, C. Jones, and G. R. Asrar, 2009: Addressing climate information needs at the regional level: The CORDEX framework. *WMO Bull.*, **58**, 175–183, https://public.wmo.int/en/bulletin/addressing-climate-information-needs-regional-level-cordex-framework.

——, and Coauthors, 2012: RegCM4: Model description and preliminary tests over multiple CORDEX domains. *Climate Res.*, **52**, 7–29, https://doi.org/10.3354/cr01018.

Gleckler, P. J., K. E. Taylor, and C. Doutriaux, 2008: Performance metrics for climate models. *J. Geophys. Res.*, **113**, D06104, https://doi.org/10.1029/2007jd008972.

Gutowski, W. J., Jr., and Coauthors, 2016: WCRP COordinated Regional Downscaling EXperiment (CORDEX): A diagnostic MIP for CMIP6. *Geosci. Model Dev.*, **9**, 4087–4095, https://doi.org/10.5194/gmd-9-4087-2016.

Haensler, A., F. Saeed, and D. Jacob, 2013: Assessing the robustness of projected precipitation changes over central Africa on the basis of a multitude of global and regional climate projections. *Climatic Change*, **121**, 349–363, https://doi.org/10.1007/s10584-013-0863-8.

Hamada, A., Y. N. Takayabu, C. Liu, and E. J. Zipser, 2015: Weak linkage between the heaviest rainfall and tallest storms. *Nat. Commun.*, **6**, 6213, https://doi.10.1038/ncomms7213.

Harris, I., T. J. Osborn, P. Jones, and D. Lister, 2020: Version 4 of the CRU TS monthly high-resolution gridded multivariate climate dataset. *Sci. Data*, **7**, 109, https://doi.org/10.1038/s41597-020-0453-3.

Hersbach, H., and Coauthors, 2020: The ERA5 global reanalysis. *Quart. J. Roy. Meteor. Soc.*, **146**, 1999–2049, https://doi.org/10.1002/qj.3803.

Hua, W., L. Zhou, H. Chen, S. E. Nicholson, A. Raghavendra, and Y. Jiang, 2016: Possible causes of the Central Equatorial African long-term drought. *Environ. Res. Lett.*, **11**, 124002, https://doi.org/10.1088/1748-9326/11/12/124002.

——, ——, S. E. Nicholson, H. Chen, and M. Qin, 2019: Assessing reanalysis data for understanding rainfall climatology and variability over Central Equatorial Africa. *Climate Dyn.*, **53**, 651–669, https://doi.org/10.1007/s00382-018-04604-0.

Huang, B., and Coauthors, 2017: Extended Reconstructed Sea Surface Temperature, version 5 (ERSSTv5): Upgrades, validations, and intercomparisons. *J. Climate*, **30**, 8179–8205, https://doi.org/10.1175/JCLI-D-16-0836.1.

Huffman, G. J., R. F. Adler, D. T. Bolvin, and G. Gu, 2009: Improving the global precipitation record: GPCP version 2.1. *Geophys. Res. Lett.*, **36**, L17808, https://doi.org/10.1029/2009GL040000.

Hung, M., J. Lin, W. Wang, D. Kim, T. Shinoda, and S. J. Weaver, 2013: MJO and convectively coupled equatorial waves simulated by CMIP5 climate models. *J. Climate*, **26**, 6185–6214, https://doi.org/10.1175/JCLI-D-12-00541.1.

Ilori, O. W., and I. A. Balogun, 2021: Evaluating the performance of new CORDEX-Africa regional climate models in simulating West African rainfall. *Model. Earth Syst. Environ.*, https://doi.org/10.1007/s40808-021-01084-w, in press.

Jackson, B., S. E. Nicholson, and D. Klotter, 2009: Mesoscale convective systems over western equatorial Africa and their relationship to large-scale circulation. *Mon. Wea. Rev.* **137**,1272–1294, https://doi.org/10.1175/2008MWR2525.1.

Jacob, D., 2001: A note to the simulation of the annual and interannual variability of the water budget over the Baltic Sea drainage basin. *Meteor. Atmos. Phys.*, **77**, 61–73, https://doi.org/10.1007/s007030170017.

——, and R. Podzun, 1997: Sensitivity studies with the regional climate model REMO. *Meteor. Atmos. Phys.*, **63**, 119–129, https://doi.org/10.1007/bf01025368.

James, R., and Coauthors, 2018: Evaluating climate models with an African lens. *Bull. Amer. Meteor. Soc.*, **99**, 313–336, https://doi.org/10.1175/BAMS-D-16-0090.1.

Janowiak, J., and P. Xie, 2011: ISLSCP II GTS gauge-based analyses of daily precipitation over global land areas. ORNL Distributed Active Archive Center Datasets, accessed March 2020, https://doi.org/10.3334/ornldaac/1001.

Jiang, Y., L. Zhou, C. J. Tucker, A. Raghavendra, W. Hua, Y. Y. Liu, and J. Joiner, 2019: Widespread increase of boreal summer dry season length over the Congo rainforest. *Nat. Climate Change*, **9**, 617–622, https://doi.org/10.1038/s41558-019-0512-y.

Jones, C., F. Giorgi, and G. Asrar, 2011: The Coordinated Regional Downscaling Experiment: CORDEX: An international downscaling link to CMIP5. *CLIVAR Exchanges*. No. 56, International CLIVAR Project Office, Southampton, United Kingdom, 34–40.

Kamae, Y., H. Ueda, and A. Kitoh, 2011: Hadley and Walker circulations in the mid-Pliocene warm period simulated by an atmospheric general circulation model. *J. Meteor. Soc. Japan*, **89**, 475–493, https://doi.org/10.2151/jmsj.2011-505.

Kanamitsu, M., K. Yoshimura, Y. Yhang, and S. Hong, 2010: Errors of interannual variability and trend in dynamical downscaling of reanalysis. *J. Geophys. Res.*, **115**, D17115, https://doi.org/10.1029/2009jd013511.

King, A. D., and L. J. Harrington, 2018: The inequality of climate change from 1.5 to 2°C of global warming. *Geophys. Res. Lett.*, **45**, 5030–5033, https://doi.org/10.1029/2018gl078430.

Kuete, G., W. P. Mba, and R. Washington, 2019: African easterly jet south: Control, maintenance mechanisms and link with southern subtropical waves. *Climate Dyn.*, **54**, 1539–1552, https://doi.org/10.1007/s00382-019-05072-w.

Legates, D. R., and C. J. Willmott, 1990: Mean seasonal and spatial variability in gauge-corrected, global precipitation. *Int. J. Climatol.*, **10**, 111–127, https://doi.org/10.1002/joc.3370100202.

Longandjo, G. N. T., and M. Rouault, 2020: On the structure of the regional-scale circulation over central Africa: Seasonal evolution, variability, and mechanisms. *J. Climate*, **33**, 145–162, https://doi.org/10.1175/JCLI-D-19-0176.1.

Malhi, Y., 2018: Ancient deforestation in the green heart of Africa. *Proc. Natl. Acad. Sci. USA*, **115**, 3202–3204, https://doi.org/10.1073/pnas.1802172115.

Morioka, Y., S. Masson, P. Terray, C. Prodhomme, S. K. Behera, and Y. Masumoto, 2014: Role of tropical SST variability on the formation of subtropical dipoles. *J. Climate*, **27**, 4486–4507, https://doi.org/10.1175/JCLI-D-13-00506.1.

Moufouma-Okia, W., and R. Jones, 2015: Resolution dependence in simulating the African hydroclimate with the HadGEM3-RA regional climate model. *Climate Dyn.*, **44**, 609–632, https://doi.org/10.1007/s00382-014-2322-2.

Munday, C., R. Washington, and N. Hart, 2021: African low-level jets and their importance for water vapor transport and rainfall. *Geophys. Res. Lett.*, **48**, e2020GL090999, https://doi.org/10.1029/2020GL090999.

NASA, 2016: Modern-Era Retrospective Analysis for Research and Applications, version 2. Goddard Earth Sciences Data and Information Services Center, accessed 12 September 2017, https://disc.gsfc.nasa.gov/daac-bin/FTPSubset.pl.

Nicholson, S. E., and J. P. Grist, 2003: The seasonal evolution of the atmospheric circulation over West Africa and equatorial Africa. *J. Climate*, **16**, 1013–1030, https://doi.org/10.1175/15200442(2003)016%3c1013:TSEOTA%3e2.0.CO;2.

——, and A. K. Dezfuli, 2013: The relationship of rainfall variability in western equatorial Africa to the tropical oceans and atmospheric circulation. Part I: The boreal spring. *J. Climate*, **26**, 45–65, https://doi.org/10.1175/JCLI-D-11-00653.1.

——, D. Klotter, L. Zhou, and W. Hua, 2019: Validation of satellite precipitation estimates over the Congo Basin. *J. Hydrometeor.*, **20**, 631–656, https://doi.org/10.1175/JHM-D-18-0118.1.

Novella, N. S., and W. M. Thiaw, 2013: African Rainfall Climatology version 2 for famine early warning systems. *J. Appl. Meteor. Climatol.*, **52**, 588–606, https://doi.org/10.1175/JAMC-D-11-0238.1.

Oort, A. H., and J. J. Yienger, 1996: Observed interannual variability in the Hadley circulation and its connection to ENSO. *J. Climate*, **9**, 2751–2767, https://doi.org/10.1175/1520-0442(1996)0092.0.CO;2.

Pokam, W. M., L. A. Djiotang, and F. K. Mkankam, 2012: Atmospheric water vapor transport and recycling in equatorial central Africa through NCEP/NCAR reanalysis data. *Climate Dyn.*, **38**, 1715–1729, https://doi.org/10.1007/s00382-011-1242-7.

——, C. L. Bain, R. S. Chadwick, R. Graham, D. J. Sonwa, and F. M. Kamga, 2014: Identification of processes driving low-level westerlies in west equatorial Africa. *J. Climate*, **27**, 4245–4262, https://doi.org/10.1175/JCLI-D-13-00490.1.

Popke, D., B. Stevens, and A. Voigt, 2013: Climate and climate change in a radiative-convective equilibrium version of ECHAM6. *J. Adv. Model. Earth Syst.*, **5** (1), 1–14, https://doi.org/10.1029/2012MS000191.

Raghavendra, A., 2020: Factors influencing rainfall over the Congo. Ph.D. thesis. State University of New York at Albany, 161 pp., https://www.proquest.com/openview/b0398896db318fc3b5411e85ef38b6f4/1? cbl=18750&diss=y&pq-origsite=gscholar.

——, L. Zhou, Y. Jiang, and W. Hua, 2018: Increasing extent and intensity of thunderstorms observed over the Congo Basin from 1982 to 2016. *Atmos. Res.*, **213**, 17–26, https://doi.org/10.1016/j.atmosres.2018.05.028.

——, P. E. Roundy, and L. Zhou, 2019: Trends in tropical wave activity from the 1980s to 2016. *J. Climate*, **32**, 1661–1676, https://doi.org/10.1175/jcli-d-18-0225.1.

Remedio, A. R., and Coauthors, 2019: Evaluation of new CORDEX simulations using an updated Köppen–Trewartha climate classification. *Atmosphere*, **10**, 726, https://doi.org/10.3390/atmos10110726.

Roeckner, E., and Coauthors, 1996: The atmospheric general circulation model ECHAM4: Model description and simulation of present-day climate. Max Planck Institute for Meteorology Rep. **218**, 171 pp.

Rowell, D. P., 2013: Simulating SST teleconnections to Africa: What is the state of the art? *J. Climate*, **26**, 5397–5418, https://doi.org/10.1175/JCLI-D-12-00761.1.

Schneider, U., A. Becker, P. Finger, A. Meyer-Christoffer, M. Ziese, and B. Rudolf, 2013: GPCC's new land surface precipitation climatology based on quality-controlled in situ data and its role in quantifying the global water cycle. *Theor. Appl. Climatol.*, **115**, 15–40, https://doi.org/10.1007/s00704-013-0860-x.

Sinclaire, Z., A. Lenouo, C. Tchawoua, and S. Janicot, 2015: Synoptic Kelvin type perturbation waves over Congo basin over the period 1979–2010. *J. Atmos. Sol. Terr. Phys.*, **130–131**, 43–56, https://doi.org/10.1016/j.jastp.2015.04.015.

Sørland, S. L., and Coauthors, 2021: COSMO-CLM regional climate simulations in the Coordinated Regional Climate Downscaling Experiment (CORDEX) framework: A review. *Geosci. Model Dev.*, **14**, 5125–5154, https://doi.org/10.5194/gmd-14-5125-2021.

Stachnik, J. P., and C. Schumacher, 2011: A comparison of the Hadley circulation in modern reanalyses. *J. Geophys. Res.*, **116**, D22102, https://doi.org/10.1029/2011jd016677.

Stevens, B., and Coauthors, 2013: Atmospheric component of the MPI-M Earth System Model: ECHAM6. *J. Adv. Model. Earth Syst.*, **5**, 146–172, https://doi.org/10.1002/jame.20015.

Taguela, T. N., and Coauthors, 2020: CORDEX multi-RCM hindcast over central Africa: Evaluation within observational uncertainty. *J. Geophys. Res.*, **125**, e2019JD031607, https://doi.org/10.1029/2019JD031607.

Tamoffo, A. T., and Coauthors, 2019: Process-oriented assessment of RCA4 regional climate model projections over the Congo Basin under 1.5°C and 2°C global warming levels: Influence of regional moisture fluxes. *Climate Dyn.*, **53**, 1911–1935, https://doi.org/10.1007/s00382-019-04751-y.

——, A. Dosio, D. A. Vondou, and D. Sonkoué, 2020: Process-based analysis of the added value of dynamical downscaling over central Africa. *Geophys. Res. Lett.*, **47**, e2020GL089702, https://doi.org/10.1029/2020GL089702.

——, G. Nikulin, D. A. Vondou, A. Dosio, R. Nouayou, M. Wu, and P. M. Igri, 2021: Process-based assessment of the impact of reduced turbulent mixing on Congo Basin precipitation in the RCA4 Regional Climate Model. *Climate Dyn.*, **56**, 1951–1965, https://doi.org/10.1007/s00382-020-05571-1.

Taylor, K. E., R. J. Stouffer, and G. A. Meehl, 2012: An overview of CMIP5 and the experiment design. *Bull. Amer. Meteor. Soc.*, **93**, 485–498, https://doi.org/10.1175/BAMS-D-11-00094.1.

Teichmann, C., and Coauthors, 2020: Assessing mean climate change signals in the global CORDEX-CORE ensemble. *Climate Dyn.*, **57**, 1269–1292, https://doi.org/10.1007/s00382-020-05494-x.

Titchner, H. A., and N. A. Rayner, 2014: The Met Office Hadley Centre sea ice and sea surface temperature data set, version 2: 1. Sea ice concentrations. *J. Geophys. Res.*, **119**, 2864–2889, https://doi.org/10.1002/2013jd020316.

Todd, M. C., and R. Washington, 2004: Climate variability in central equatorial Africa: Influence from the Atlantic sector. *Geophys. Res. Lett.*, **31**, L23202, https://doi.org/10.1029/2004GL020975.

Toniazzo, T., and S. Woolnough, 2013: Development of warm SST errors in the southern tropical Atlantic in CMIP5 decadal hindcasts. *Climate Dyn.*, **43**, 2889–2913, https://doi.org/10.1007/s00382-013-1691-2.

Vondou, D. A., and A. Haensler, 2017: Evaluation of simulations with the regional climate model REMO over Central Africa and the effect of increased spatial resolution. *Int. J. Climatol.*, **37**, 741–760, https://doi.org/10.1002/joc.5035.

Wahl, S., M. Latif, W. Park, and N. Keenlyside, 2009: On the tropical Atlantic SST warm bias in the Kiel Climate Model. *Climate Dyn.*, **36**, 891–906, https://doi.org/10.1007/s00382-009-0690-9.

Washington, R., R. James, H. Pearce, W. M. Pokam, and W. Moufouma-Okia, 2013: Congo Basin rainfall climatology: Can we believe the climate models? *Philos. Trans. Roy. Soc. London*, **B368**, 20120296, https://doi.org/10.1098/rstb.2012.0296.

Weber, T., A. Haensler, and D. Jacob, 2017: Sensitivity of the atmospheric water cycle to corrections of the sea surface temperature bias over southern Africa in a regional climate

model. *Climate Dyn.*, **51**, 2841–2855, https://doi.org/10.1007/s00382-017-4052-8.

——, ——, D. Rechid, S. Pfeifer, B. Eggert, and D. Jacob, 2018: Analyzing regional climate change in Africa in a 1.5, 2, and 3°C global warming world. *Earth's Future*, **6**, 643–655, https://doi.org/10.1002/2017EF000714.

Zhao, S., and K. H. Cook, 2021: Influence of Walker circulations on East African rainfall. *Climate Dyn.*, https://doi.org/10.1007/s00382-020-05579-7.

Zhou, L., and Coauthors, 2014: Widespread decline of Congo rainforest greenness in the past decade. *Nature*, **509**, 86–90, https://doi.org/10.1038/nature13265.